129Xenon NMR: Review of Recent Insights into Porous Materials

Erika Weiland, Marie-Anne Springuel-Huet, Andrei Nossov, Antoine Gedeon

^{129}Xenon NMR: Review of Recent Insights into Porous Materials

Erika Weiland[1,2], Marie-Anne Springuel-Huet[1], Andrei Nossov[1], Antoine Gédéon[1]*

[1] Sorbonne Universités, UPMC Univ Paris 06, CNRS-UMR 7574, Laboratoire de Chimie de la Matière Condensée de Paris, 11 place Marcelin Berthelot, F-75005, Paris, France

[2] IFP Energies nouvelles, Etablissement de Lyon – Rond-point de l'échangeur de Solaize- BP3, -69360 Solaize – France

* corresponding author

e-mail adresses : erika.weiland@gmail.com, marie-anne.springuel-huet@upmc.fr, andrei.nossov@upmc.fr, antoine.gedeon@upmc.fr

Abstract

This paper presents a comprehensive review of the recent advances in xenon -129 nuclear magnetic resonance (NMR) measurements.

In the past thirty years, ^{129}Xe NMR has proved to be an efficient technique to investigate the structure of porous solids and several extensive reviews on the subject are available in the literature. The main advantage of ^{129}Xe NMR is the high sensitivity of the xenon atom to its local environment. Using optical pumping techniques for the production of hyper- polarized (HP) xenon has led to an increase in sensitivity of several orders of magnitude. This development has opened the way to explore the internal structure and the porosity of a wide range of new advanced materials.

This review which covers the period, 2005 up to now, starts with a description of the basic theory of xenon- NMR. It presents a basic overview of thermally and polarized

xenon NMR technique followed by the recent NMR developments on various classes of porous materials.

Keywords

^{129}Xe NMR, hyperpolarized xenon, porous materials

1. Introduction

The xenon element, named after ξένον, a Greek word meaning « foreign », was discovered by Ramsay and Travers on July 12, 1898 during their experiments of fractionating liquid air. Xenon is more reactive and much rarer than the other noble gas. It is colourless, odourless and non-flammable.

In 1916 and 1932, Kossel and Pauling, respectively predicted that xenon can react with strong oxidants. This was confirmed in 1962, when Neil Bartlett observed that xenon reacted with vapours of platinum hexafluoride (PtF_6) to form a yellow–orange solid compound. This discovery was recognized as one of the most significant inorganic chemistry advances of the twentieth century.

Xenon can form various fluorides, oxides and perxenates (XeO_6^{4-} salts), bonds to carbon and nitrogen, and can also coordinate metal ions, as shown by the recent synthesis of a compound with gold ($AuXe_4^{2+}$) [1]. Xenon now finds uses in fields as various as lasers and incandescent lamps, plasma display panels, silicon etching in semiconductor manufacturing and medicine. In 2008, twelve million liters of xenon were extracted from the atmosphere and the production is growing to meet technological needs. One of the most exciting new applications is the xenon-ion propulsion of spacecraft engines for space travel. Initially deemed unreactive, xenon is now finding ways to come out of its shell [2].

The first ^{129}Xe NMR experiments were realized in 1951 when Proctor and Yu reported the magnetic moment of the isotope [3]. In the early 80s, ^{129}Xe NMR spectroscopy of adsorbed xenon was proposed as an approach to study the pore structure of zeolites and clathrates [4,5]. The main concept of this technique is that the chemical shift of the Xe atom is extremely sensitive to the local environment and to chemical factors such as the

composition of the material, the nature and concentration of co-adsorbed molecules, and the shape and size of host void spaces.

The historical development of ^{129}Xe NMR, in particular the first contributions on porous materials, is summarized in Figure 1.

During the last 35 years, ^{129}Xe NMR spectroscopy has been applied on various systems, such as porous materials, systems with supported metals [6–11], polymers [12–18], biomolecules [19–23], liquid crystals [24–28] etc. Important theoretical developments have been performed for a better understanding of the NMR chemical shift and line shapes of ^{129}Xe [28–34].

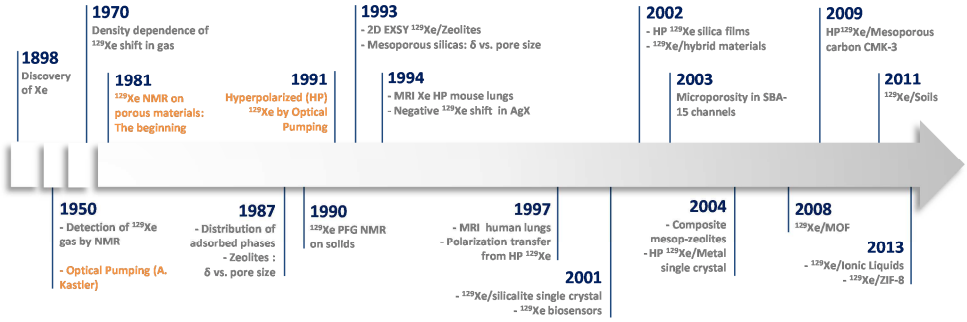

Figure 1 : Historical timeline of ^{129}Xe NMR with important dates and events.

Unlike conventional ^{129}Xe NMR in which the nuclear spin polarization is governed by Boltzmann equilibrium [35,36], laser-polarized so-called hyperpolarized (HP) ^{129}Xe NMR became feasible thanks to a polarization transfer from alkali-metal electronic spins to ^{129}Xe nucleus by the spin-exchange optical-pumping method (SEOP), thus capable of enhancing signal sensitivity by a factor of 10^3–10^5 folds even at dilute Xe loading. This enhancement has allowed an extension of the xenon NMR experiments to novel applications of NMR and MRI in chemistry, materials science and biomedicine. 2D exchange spectroscopy (EXSY) of CF (continuous flow) HP ^{129}Xe NMR were also

used in order to obtain a better understanding of the pore structure, the distribution of the adsorption sites and the pore network interconnectivity between different adsorption regions [37–39].

The use of ^{129}Xe NMR spectroscopy to study porous materials is now a well-established method that has been reviewed several times [40–46]. In this comprehensive review which covers essentially more recent literature, we first describe the theory and the basic idea behind xenon NMR in porous materials, then, the pathways used to produce hyperpolarized xenon and, finally, highlight the applications of xenon adsorbed in different types of innovative porous materials.

2. Basic principle of ^{129}Xe NMR spectroscopy of xenon adsorbed on porous materials

Xenon is a monoatomic inert gas with a van der Waals diameter of 4.4 Å. It has more than 50 isotopes, including nine stable ones. NMR experiments can exploit two isotopes of xenon, ^{129}Xe (I=1/2) and ^{131}Xe (I=3/2) with a natural abundance of 26.4% and 26.2%, respectively. However, for most NMR experiments ^{129}Xe is more frequently used mainly because of the complexity of spectra due to the high quadrupolar moment of the ^{131}Xe isotope. Any distortion of the large highly-polarizable electron cloud of the xenon atom is directly transmitted to the nucleus, affecting the chemical shift. This high polarizability is reflected in a wide chemical shift range (about 7,000 ppm). The range goes from -40 ppm for Xe adsorbed in AgX to almost 1000 ppm in CoY zeolites or is much wider if chemical compounds of xenon are considered (from -740 ppm for the Re(iPrCp)(CO)(PF3)Xe complex to 6200 ppm for the XeO_2F^+ cation [47–50].

2.1. Experimental observations

In their first pioneering NMR studies of xenon adsorbed on different kinds of zeolites, Fraissard and coworkers have shown that the chemical shift of adsorbed xenon is highly influenced by the size of the cavities [51,52] and the nature of metal ions into the zeolite framework [53]. Furthermore, they have shown that the chemical shift of xenon strongly depends on the surface heterogeneity, the structure defects, and the distribution of coadsorbed phases. Actually, the measured ^{129}Xe NMR shifts reflect the lifetime of the xenon atoms on each adsorption site.

In the absence of strong adsorption sites, the chemical shift, δ, of a xenon atom adsorbed in a pore can be presented as the sum of terms corresponding to the different perturbations to which the atom is subjected:

$$\delta = \delta_0 + \delta_s + \delta_{Xe} \qquad \text{Equation 1}$$

where δ_0 is the chemical shift of xenon gas at zero pressure (reference), δ_s is the contribution due to interaction with the pore surface. This term can reflect the geometry of the xenon environment on the surface. The contribution δ_{Xe} is due to xenon – xenon collisions inside the pore. This term is proportional to xenon density and, thus, increases with the xenon concentration.

This increase in chemical shift with the xenon pressure is typical for microporous solids. For zeolites, the chemical shift increases because of important Xe–Xe interactions due to confinement inside the micropores (pore size below 20 Å). In the usual pressure range studied, the influence of the pressure on δ is however negligible for purely mesoporous solids (pore size above 20 Å) because the Xe-Xe interactions inside the mesopores are similar to that in the gas phase. In gas phase, the increase in chemical shift with pressure is rather weak: 0.55 ppm/amagat (1 amagat being the concentration of Xe under standard conditions) [54].

2.2. Fast exchange model

Under fast exchange conditions between Xe adsorbed on the surface and xenon gas inside the pore, and assuming that the adsorption isotherms of xenon on mesoporous materials obey Henry's law (at least when the xenon pressure is not too high), the ^{129}Xe chemical shift of xenon adsorbed on mesoporous materials is expressed as [55]:

$$\delta = \frac{\delta_a}{1+\frac{V}{KSRT}} \quad \text{Equation 2}$$

where δ_a is the chemical shift of xenon in the adsorbed phase, V is the mesoporous volume, S the mesopore surface area, T the temperature and K the Henry constant. This relationship shows that the observed chemical shift does not depend upon the equilibrium pressure. Knowing K and δ_a, it is possible to obtain the volume-to-surface ratio, V/S. This relation between δ and the local volume-to-surface ratio can also be written as a function of pore size:

$$\delta = \frac{\delta_a}{1+\frac{D}{b}} \quad \text{Equation 3}$$

where the pore diameter $D = \eta V/S$, $b = \eta KRT$ and η depends on the geometry model adopted for the pores. In this case the dimensions of the pore can then be deduced.

The Henry constant K, which is temperature dependent, can be written as:

$$K = \frac{K_0}{\sqrt{T}} e^{-\frac{\Delta H}{RT}} \quad \text{Equation 4}$$

where K_0 is the pre-exponent factor which does not depend on the temperature.

Equation 2 becomes [55]:

$$\delta = \frac{\delta_a}{1+\frac{D}{\eta K_0 R\sqrt{T}}} e^{-\frac{\Delta H}{RT}} \quad \text{Equation 5}$$

Measuring the chemical shift as a function of temperature allows obtaining the effective heat of adsorption, ΔH, or enthalpy of xenon adsorption for the solids under

consideration. However, the temperature should not be too low in order that the adsorption of xenon and hence, xenon-xenon interactions in the adsorbed layer remain negligible.

2.3. Impact of xenon diffusion and the presence of strong adsorption sites on ^{129}Xe NMR chemical shift

The intra- and intercrystallite diffusion of xenon may also play a role and must be taken into account. If, on the NMR time scale (typically of the order of ms), Xe diffuses within several crystallites, it does not only report on its sampling of the inside environment of a single crystal but also of that of many crystallites as well as that of the interparticle space. The chemical shift is then averaged and may be not truly characteristic of the porosity of the solid studied. The influence of intercrystallite diffusion depends on the size and morphology of the crystallites, the pore size, the crystallite packing, the Xe gas pressure and the temperature [56,57].

Porous catalysts containing additional phases (e.g. metal particles [58]), highly charged cations [59], may present strong adsorption sites on their surface. These latter can specifically interact with Xe. The presence of such species is revealed in the chemical shift variations with Xe concentration. At low xenon loadings, the corresponding curves show a typical hyperbolic shape. As the concentration decreases, the chemical shift increases since, at low concentration, the Xe atoms mainly interact with these species. Then, one should write an additional term, δ_{SAS}, in Equation 1which becomes:

$$\delta = \delta_0 + \delta_s + \delta_{Xe} + \delta_{SAS} \qquad \text{Equation 6}$$

Generally speaking, the equation contains as many terms as there are different kinds of interaction between the Xe atoms and the material.

If all interactions of the Xe atoms with the materials are essentially anisotropic, the NMR signals are nevertheless isotropic most of the time due to rapid exchange of the Xe atoms between different sites. In small pores presenting anisotropic environments (small channels or oblate cavities), in which the xenon atoms undergo anisotropic interactions, the shape of the signals reflects the symmetry of the pores. For example, it is the case for the alumino-phosphate AlPO-11 which presents unidimensional channels with elliptical cross section (4.0×6.5 Å) [60,61], clathrate cages [5], or even tri-dimensional channel system in ZSM-5 macro-crystals [57,62].

3. Hyperpolarization of Xenon nuclei

At the beginning of the use of ^{129}Xe NMR to study porous solids in the late 70s and then, during the 80s, the experiments were performed with conventional NMR (that is with thermally-polarized spin nuclei). As long as microporous solids (such as zeolites or clathrates) with high adsorbtion capacity of xenon were studied, the low sensitivity of NMR was not a huge handicap. Nevertheless, the extension of this technique to other materials was limited due to the low spin polarization of the ^{129}Xe nuclei.

Successful attempt of Pines and coworkers to polarize ^{129}Xe nuclei via optical pumping of gaseous Rb atoms [63] revolutionized the area of xenon spectroscopy and imaging, greatly extending the use of ^{129}Xe NMR to study materials with low surface area, long relaxation time or in very small quantity (films). The rather long-living van der Waals Xe-Rb pairs formed in gas phase allow the transfer of the Rb electronic polarisation to the ^{129}Xe nuclei. The magnetization of ^{129} Xe in such experiments can easily reach several percent (even tens of percent with high-end devices) versus ca. 10^{-5} values, typical for experiments with thermally polarized at ambient temperature.

3.1. Spin Exchange optical Pumping (SEOP)

The two most common approaches to HP-^{129}Xe via Spin-Exchange Optical Pumping (SEOP) are named continuous flow and batch modes [64–66]. The first polarizing systems were operating in batch mode, when a certain amount of polarized gas was admitted to a sample tube containing the absorbent. Prompt implementation of continuous flow systems greatly improved the convenience and productivity of HP experiments regardless the fact that polarization levels in batch systems were much higher than those obtained under flow conditions. The first paper reporting continuous-flow SEOP in aerosil surface was published by Haake *et al*. [67] In such systems a Xe-He mixture is passed first through the pressurized polarizing cell containing Rb vapor and then through the sample. The mixture containing ca. 1% of xenon can be conveniently released into atmosphere or can be forced to circulate in the system, which is more rational in experiments with higher partial Xe pressure in the mixture. A schematic representation of continuous flow setup is given in Figure 2.

The glass cell containing a small amount of Rb is heated to 100-150 °C and placed in a fringe field of NMR magnet or in Helmholtz coils. The cell is irradiated by a circularly-polarized light from laser diode arrays with a wave length of 794.7 nm corresponding to the D_1 transition of Rb. A water refrigerant is connected to the cell to prevent Rb vapor to be dragged along the PFA tubing connecting the cell with the sample tube. A near-IR spectro-photometer is placed behind the Rb cell with respect to the laser source in order to check the polarization process by analysis of the transmitted light.

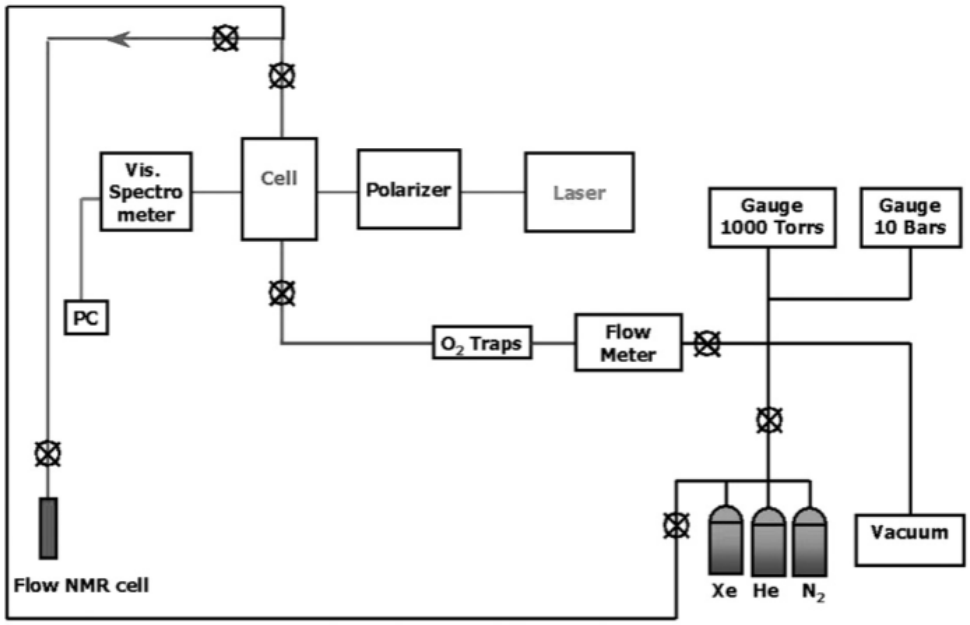

Figure 2. Schematic representation of continuous flow system for production of hyperpolarized ^{129}Xe. From reference [37] with permission.

The system described above can be easily accommodated for flow NMR spectroscopy (including magic angle spinning, MAS, experiments) as well as for cryo collecting of polarized gas for purposes of xenon MRI. The first application of HP xenon under MAS experiments was described by Brunner *et al*. [68]. However, to perform MAS experiments with hyperpolarized ^{129}Xe under continuous flow, MAS probes can be adapted. One example is the following. Starting from a standard Bruker 7 mm MAS probe, a PFA capillary tube is accommodated inside the probe to ensure the injection of the gas mixture [69]. It is connected to a glass tube which delivers the gas mixture to the sample, carefully packed inside a 7 mm rotor, through a hole drilled in the rotor cap. The gas mixture is not collected after passing through the powder and, under this lost-flow condition, the rotors can spin at speeds up to 3.5 kHz.

3.2. Other ^{129}Xe polarizer designs

One of the first design for a spin-exchange optical pumping system to produce large amount of HP xenon was reported by Ruset *et al.* [70]. Working at low pressure in batch [70] or in continuous flow [71] modes, the systems allow having a large spin-exchange rate between Rb and ^{129}Xe resulting in short residence times for the Xe/Rb gas mixture and large HP xenon production. Then, other ^{129}Xe polarizer designs have been developed [72,73] over the past decades, including an open-source clinical-scale prototype [72,74] and the 3D-printed hyperpolarizer [75,76]. These systems can deliver near-unity ^{129}Xe polarization levels. However, the polarizations obtained via spin-exchange are limited at high xenon concentration in the pumping cell. Volume holographic grating, VHGs, have been intensively investigated and developed for applications in spectroscopy. By narrowing the spectral output of high-power laser-diode arrays (LDA), it was possible to reach a 3-fold improvement in ^{129}Xe nuclear polarization even at high in-cell xenon densities [77,78]. In addition to the utility of VHG narrowed lasers, it was reported that there is an inverse relationship between the xenon partial pressure and the optimal cell temperature of the Rb/Xe SEOP. This interdependence was exploited to obtain a very high ^{129}Xe polarization in high in-cell xenon densities [77].

An automated hyperpolarizer has been designed by Nikolaou *et al.* to be readily implementable in a lab for MRI measurements. This device runs with a 20 W laser at the Rb D_1 line and up to 1800 Torr of Xe in 50 cm^3 in batch or continuous flow modes [72]. A temperature-ramped SEOP in batch mode was also performed in order to have quick increase in spin polarization, high level of Xe polarization and low Rb gas content [79].

In 2013, Korchak *et al.* developed a ^{129}Xe polarizer housed in a mobile frame [80]. This polarizer can be used in batch or flow modes for spectroscopic or small animal applications.

3.3. Alternative methods to produce HP-Xenon

(a) DNP method

In addition to the spin exchange optical pumping (SEOP) technique, an alternative method to produce hyperpolarized xenon gas uses dynamic nuclear polarization (DNP) [81]. This technique, performed at very low temperature, allows enhancing the polarization of nuclei in samples containing paramagnetic centers. The large electron spin polarization is transferred to the nuclear spin system by irradiation with microwaves at or near the electron Larmor frequency.

Recently, Capozzi *et al.* [82] has proposed a DNP method to hyperpolarize Xe nuclei, at very low temperature, using different organic solvents and TEMPO radical (Figure 3). The polarization is maintained after the sublimation of the medium and can be subsequently used for MRI applications. The intrinsic advantage of DNP over SEOP is that the volume of xenon which can be produced in a single experiment is potentially much larger due to higher density of solid xenon as compared to the xenon gas phase.

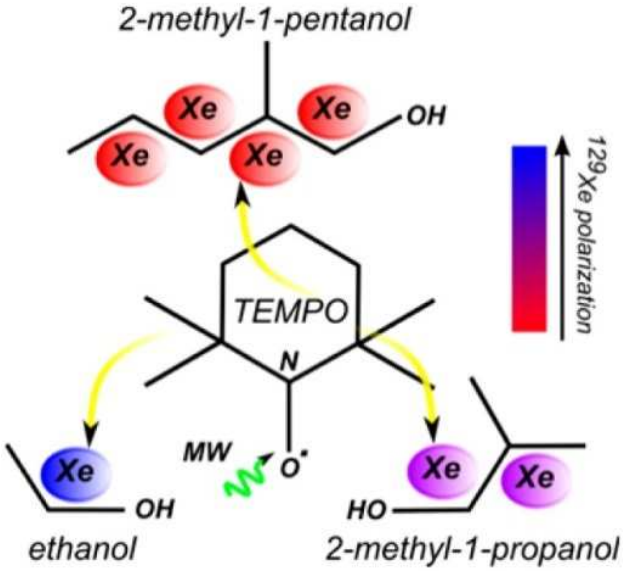

Figure 3. Schematic representation of polarization transfer from TEMPO radical to Xe nuclei. From reference [82] with permission.

b) Cryogenic or brute force method

Cryogenic or brute force method proposed by Krjukov *et al.* can also be used for producing hyperpolarized xenon [83]. According to this method, xenon was held at very low temperature (below 25 mK) in a high magnetic field (14.7 T). The main barrier for the brute force method is the very long spin lattice relaxation time for xenon solid at very low temperature. To overcome this obstacle, Honig *et al.* have used oxygen as a relaxant molecule which leads to an effective relaxation of xenon at low temperatures [84,85]. Helium (^{3}He) was also used a relaxant agent [86]. The advantage of ^{3}He is that it could be easily removed from the sample without much loss of xenon polarization. In their experiments on silica gel, O'Neill *et al.* have succeeded to distinguish the NMR signal arising from xenon atoms in the upper monolayers from that of Xe atoms in the lower monolayer on the silica gel surface [87].

4. Xenon as a probe of micropourous solids

Crystalline microporous solids, as zeolites, are an important class of inorganic materials with uses in different areas impacting our everyday lives, namely as catalysts, adsorbent, and ion exchangers. These materials have been widely studied in terms of relations among structure, properties and catalytic activity. Pillared clays are an interesting class of 2-dimensional microporous materials. Due to their high surface area and permanent porosity they are very attractive solids for adsorption and catalysis purposes.

4.1. Xenon NMR applied on zeolites

In the 80s and 90s, ^{129}Xe NMR has been extensively used to study zeolite pore structures. The various values of the chemical shift observed for many different structures allowed some of us to establish a relationship between the chemical shift δ_s (obtained by extrapolating, at zero Xe loading, the chemical shift measured as a function of Xe pressure) and the pore dimension, via the mean free path of a Xe atom diffusing in the pores [88]. Analogous relationship has been obtained later for mesoporous silica and silica-alumina materials [89].

In more recent years, the progress in computer calculation has made the determination of solid structures from X-ray diffraction experiments much easier and ^{129}Xe NMR has been less applied to study the pore structures of zeolites. However, the technique has still been used in the zeolite domain, for example to investigate the nucleation or the structure collapse under severe treatments or the location of extraframework species such as metal clusters or oxides. In the case of zeolites obtained in the form of nanocrystals or nanosheets, XRD diffraction cannot be used and ^{129}Xe NMR still remains very useful to give information on the pore structures.

4.2. Pore size and connectivity

Knagge *et al.* analyzed the porosity of porous silicon using hyperpolarized ^{129}Xe NMR [39]. The spectra exhibit two signals of adsorbed xenon attributed to two types of pores. Using the relationship between the chemical shift and the pore size related to silicas [89], they could determine the mean pore size of the pores, namely 9.5 and 18.5 nm. 2D MAS EXSY experiments were performed to investigate the exchange of Xe between the two types of pores. To get rid of the HP xenon arriving in the rotor after the first pulse of the sequence that would affect the peak intensity during the whole sequence, they implemented a specific phase cycling and additional 180° pulse in the usual pulse sequence. Rate constants for exchange between the different pores themselves and with the gas phase have been evaluated.

4.3. Monitoring zeolite nucleation / collapse

The crystallisation of zeolites takes place in two kinds of systems: hydrogel systems containing bulk solid and liquid parts or "clear solutions" containing discrete, well-defined gel particles. The number of these particles is limited in clear solution and such systems have been chosen by numerous groups to study zeolite crystallisation. However, all industrially-synthesized zeolites are obtained from hydrogel systems. In this respect, the understanding of processes taking place in zeolite-yielding gel-rich systems is much less known than their highly-diluted counterparts. The events preceding zeolite nucleation in sodium-rich aluminosilicate hydrogel precursors are even less known.

To study such complex systems, many characterisation techniques are necessary. For example Valtchev's group has used a combination of hyperpolarized (HP) ^{129}Xe NMR with N_2 adsorption, high resolution transmission spectroscopy, energy-dispersive

spectrometry, X-ray diffraction, infrared spectroscopy, scanning electron microscopy and chemical analyses to study the changes in composition and structure of sodium hydroxide rich aluminosilicate gel during the synthesis of zeolite A [90]. Many years ago, it has been shown that xenon adsorbs in NaA zeolite only under high pressure (several atmospheres) and at high temperature. In this zeolite the Na cations are located near the windows (4.1 Å wide) preventing Xe atoms from diffusing through the α-cavities at room temperature and low pressures [91]. The resulting feature is that, after Xe is adsorbed under proper conditions, the spectrum recorded at room temperature shows several lines corresponding to the different Xe populations in the cavities, since the chemical shift depends on the number of Xe atoms in the cavities. This interesting case gave rise to a great number of experimental and theoretical studies on Xe NMR shift [30,92–97].

In the study of Valtchev's group, the samples underwent a cationic exchange to obtain the calcium form before characterization. In principle the Xe atoms diffuse easily between the cavities since one half of the windows are free from cation and the spectrum contains only a single line due to the averaging of chemical shifts corresponding to the different populations inside the cavities. Even at 144 K, a single line is observed for a mean Xe loading of 8 atoms per cavity [98]. Nevertheless, the spectra of pure CaA sample obtained after 300 min of synthesis show several lines that were attributed to different populations in the cavities. The presence of these lines in the spectra of samples obtained at intermediate synthesis times is used as a signature of the presence of crystals of A zeolite. One may remark that, the observation of these multiple lines for CaA may be due to a partial exchange of Na^+ cations by Ca^{2+} ones, allowing

Xe atoms to adsorb in the zeolite but not to diffuse very rapidly between the cavities at low temperatures.

Snears *et al.* have reported interesting HP ^{129}Xe NMR results concerning the formation of porous aluminophosphates frameworks during the synthesis of AlPO-18 [99]. The spectra clearly show the formation of AlPO-5 network at intermediate stages of synthesis (Figure 4). Moreover, to provide insight into the pore connectivity, the dynamics of Xe atoms have been investigated by 2D EXSY NMR on the solid containing the two structures (Figure 5). The presence of cross-peaks indicates an exchange occurring at the smallest mixing time (t_{mix} = 1 ms) between the two structures. The Xe atoms also exchange between AlPO-5 and the free gas at t_{mix} = 5 ms but not between AlPO-18 and the gas whereas an exchange is observed for t_{mix} = 5 ms in a pure AlPO-18 solid. This suggests that the AlPO-18 phase is formed in the core of AlPO-5 particles.

^{129}Xe NMR has been used not only to monitor the zeolite synthesis but also to follow the zeolite collapse under severe conditions [100].

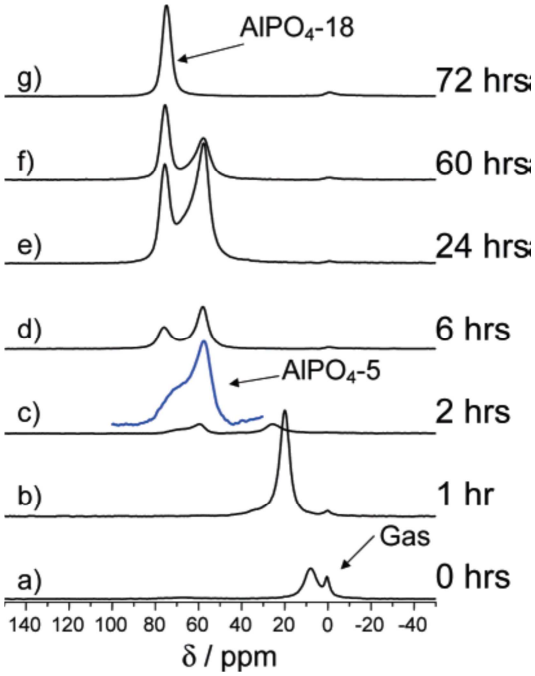

Figure 4. ^{129}Xe NMR spectra of hyperpolarized xenon in calcined aluminophosphate samples after various heating times. The inset in c (after heating for 2 hrs) is an expansion (×10 vertical magnification) of the peak centered at $\delta_{iso} \approx 63$ ppm. From reference [99] with permission.

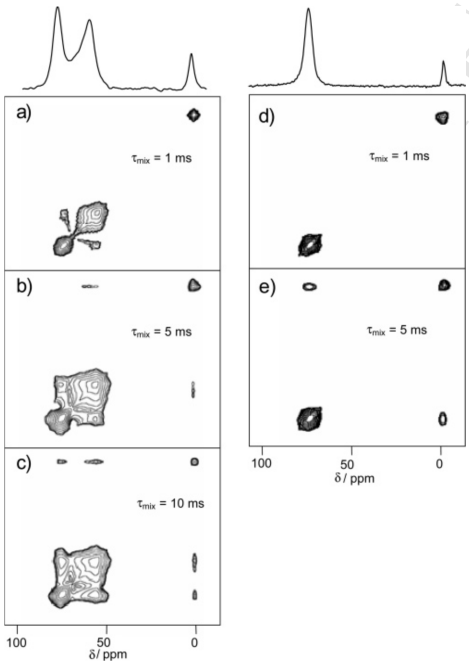

Figure 5. Left column, ^{129}Xe 2D-EXSY spectra of the sample heated for 24 h at three different mixing times: (a) t_{mix} = 1 ms, (b) t_{mix} = 5 ms, and (c) t_{mix} = 10 ms. The

corresponding 1D spectrum collected at the same time as the 2D-EXSY spectra were acquired (32 scans) is shown at the top. Right column, the ^{129}Xe 2D-EXSY spectra of xenon adsorbed in pure AlPO4-18 at two different mixing times: (d) t_{mix} =1 ms and (e) t_{mix} = 5 ms. From reference [99] with permission.

The synthesis of zeolite, like high silica ZSM-35 (FER), may be facilitated by adding non-calcined MCM-49 (MWW) seeds to the initial gel without the presence of organic structure-directing agents [101]. The authors proposed an interface-induced growth mechanism based on Xe NMR results.

4.4. Delamination of zeolites

To expand the use of zeolites as catalysts for reactions involving large molecules, the group of Corma has developed a new approach [102]. It consists in the synthesis of layered zeolite precursors which are subsequently swollen (by exchange with bulky cations) and finally exfoliated using ultra-sounds in order to make the potentially active sites accessible at the external surface. For large reactants, delaminated zeolites show higher activity than conventional large-pore acid zeolites, AlMCM-41 mesoporous solids or amorphous silica-alumina [103].

In the case of ITQ-2, obtained from the delamination of MCM-22 zeolite, NMR spectra exhibit additional lines, compared to the single line obtained for MCM-22, at high pressures or at low temperatures (Figure 6) [104]. ITQ-2 consists of nanosheets, ca. 2.5 nm thick. A 10-membered-ring channel system runs inside the elementary layer between "cups" (0.7 nm deep) which open to the surface on both sides [102]. Within these nanoscale particles, there is a fast exchange between free and adsorbed xenon and the observed chemical shift is a weighted average of the respective chemical shifts.

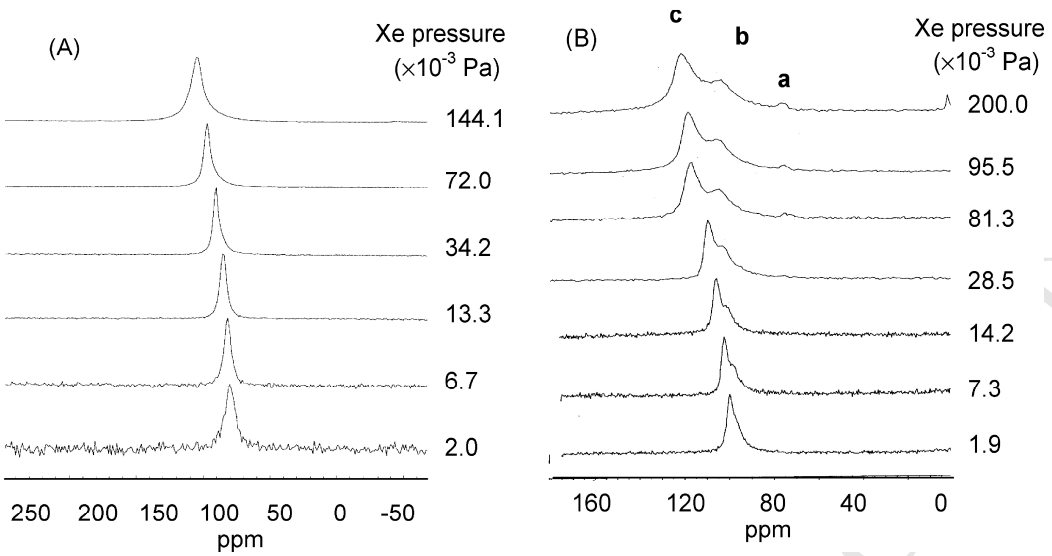

Figure 6. ^{129}Xe NMR spectra of MCM-22 (A) and in ITQ-2 (B) at 293 K for various xenon pressures. From reference [104] with permission.

The additional lines, at lower chemical shift, have been attributed to nanosheets consisting of different numbers of elementary layers and, therefore, whose particle size varies in a discrete way. At room temperature and at low pressure, Xe atoms sample particles of different sizes within the NMR timescale and spectra exhibit a single line. As the mobility of Xe atoms decreases, the exchange between gaseous Xe and Xe adsorbed in particles becomes dependent on the sizes. Since the size of particles is a low multiple of the layer size, the time spent by Xe in particles varies in a discrete way. As a consequence, the chemical shift depends on the particle size. Thus, it becomes possible to distinguish the particles according to their sizes. This interpretation has been clearly demonstrated by compressing the loose powder in order to reduce the interparticle space and consequently the exchange with the interparticle gaseous Xe. Then, the spectra show only one line whose chemical shift variation with pressure is practically identical

to that of MCM-22 proving that ITQ-2 and MCM-22 has the same pore structure. The two materials only differ from the particle size.

In the case of ITQ-6 which originates from the delamination of ferrierite zeolite, the spectra also show, in addition to the two lines corresponding to the FER pores, low-shifted lines which were attributed to mesopores. 2D EXSY MAS NMR spectra to study the exchange of the FER lines with the mesopores were recorded at various mixing times. The presence of some off-diagonal peaks allowed the authors to propose that the delamination of ferrierite is not complete and occurs at the edge of the particles, with the FER structure being maintained in the core of the material (Figure 7).

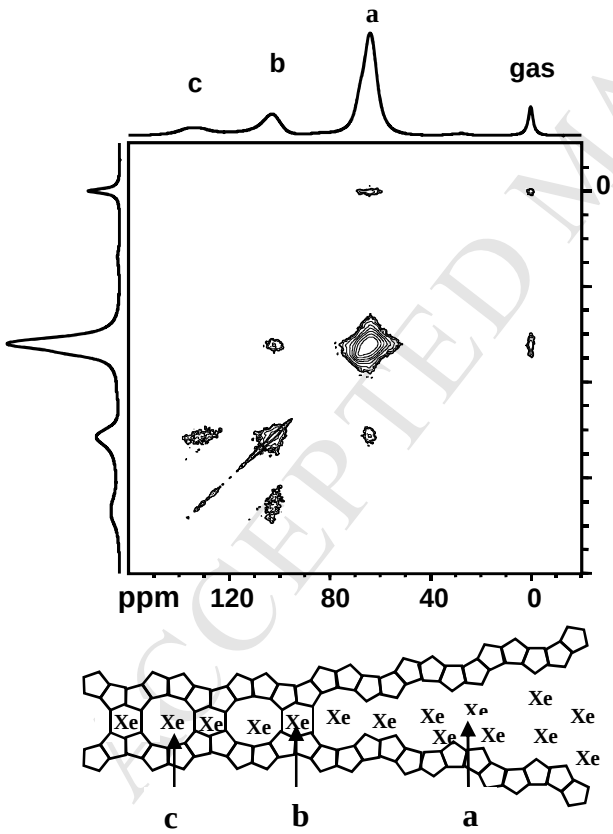

Figure 7. 2D EXSY MAS NMR spectrum of HP ^{129}Xe adsorbed on ITQ-6 (mixing time 50 ms). Sample was rotated at 3 kHz. P(Xe) ≈ 1.06×10^3 Pa. Sketch of partially delaminated ITQ-6 particles. From reference [104] with permission.

4.5. Location of extraframework species

Many products are obtained by bifunctional catalysis. In petrochemistry, bifunctional catalysts essentially consist in metal supported on zeolites. The high acidity of zeolite is responsible of cracking and isomerisation reactions and the metallic phase is responsible of hydrogenation/dehydrogenation reactions. The goal is then to introduce particular chemical species, such as cations, metal particles or oxides inside the zeolite pores. Various techniques have been developed to incorporate the desired species inside the pores as vapour deposition, impregnation etc. It is therefore of interest to check if the species have suitably been deposited within the pores. As it was reported in the past, ^{129}Xe NMR appears to be an appropriate technique to investigate the location of the species in the zeolite [7,105–116].

In the last years, a few papers deal with this subject. One concerns cerium-modified mordenite catalyst in the tert-butylation of toluene [117]. The cerium-modified mordenites have lower catalytic activity than that of parent mordenite but enhanced selectivity for para tert-butyltoluene. These modified catalysts show the same spectra as that of the parent mordenite whatever the cerium content (0 to 6% in mass) proving that cerium is essentially located on the external surface where it deactivates the external acid sites for the alkylation of toluene.

Heterogeneous catalysts for olefin metathesis reactions are based on supported Re, W or Mo. Li *et al.* obtained high catalytic performance of Mo supported on HBeta-Al_2O_3 composites for the metathesis of ethane and butane-2 to propene. Variable-temperature HP ^{129}Xe NMR experiments show that the Mo species are preferably located on Al_2O_3 rather than in the H-beta zeolite. It was concluded that this particular location is responsible of the high performance of the catalyst [118].

Another example is found in References [119,120] and concerns Fe-modified ZSM-5 catalysts extensively used in the selective reduction of nitrogen oxides which contribute to the ozone clouds and acid rain formation. The authors compared the catalytic performances of Fe-ZSM-5 catalysts obtained by impregnation in organic media (OMI) using iron acetyl acetonate with that of reference catalysts prepared by chemical vapour deposition (CVD) or impregnation in aqueous media (WMI). The chemical shift and the linewidth are both affected by the presence of Fe particles, but not too severely compared to what can be expected due to the ferromagnetism of Fe. The chemical shift deviation, compared to H-ZSM5, of the OMI and CVD catalysts is larger than that of WMI catalyst. This observation is in agreement with the results of small angle X-ray scattering experiments which show that the Fe particles have dendritic shapes for OMI and CVD catalysts. This suggests that the Fe particles are formed in the ZSM-5 channels and the geometry of Fe particles is a consequence of pore shape. The particles are then located, at least partly, in the porosity and can interact with Xe. Due to the ZSM-5 pore dimensions (5.3×5.6 and 5.1×5.5 Å), the Xe atoms cannot adsorb in channels containing Fe particles. Therefore the amount of adsorbed Xe is reduced, particularly in OMI and CVD catalysts as seen in the adsorption isotherms of Xe. Moreover, the interaction between Xe and Fe is limited and may explain the small effect of Fe on the chemical shift.

4.6. Xenon capture on silver-Loaded zeolites

Due to the several uses of xenon including commercial lighting, medical applications as imaging, anesthesia, and neuro-protection, capture of Xe has been widely investigated. In the early 1970s, Xe was found to exhibit strong interaction with silver-exchanged zeolites. In the frame of The Comprehensive Nuclear Test Ban Treaty (CTBT), nuclear

tests which produce a large amount of radioactive Xe are monitored. In order to develop more efficient detectors, the quantification of the number and strength of silver adsorption sites, for Xe atoms, in silver-exchanged zeolites, NaX, NaY, BEA and ZSM-5 have been investigated by Xe isotherms and ^{129}Xe NMR experiments [121].

4.7. Pillared Clays

Pillared structure of TEA-hectorite consists of inorganic pockets of two tetrahedral silicate layers (yellow) condensed to a central magnesium oxide octahedral layer (blue) intercalated by tetraethylammonium cations (see Figure 8). Interlayer nanoporosity of pillared hectorite was explored by hyperpolarized xenon NMR demonstrating the open pore accessibility of the structure to gases [122].

Continuous-flow hyperpolarized ^{129}Xe NMR spectra of xenon diffusing in the interpillar structure of TEA-hectorite at variable temperature are shown in Figure 8. At room temperature the signal at 105 ppm, is indicative of the gas confined to the restricted spaces. Lowering the temperature causes the Xe resonance to shift linearly downfield, up to 144 ppm, indicating increasing condensation of xenon on the micropore surface. Below 205 K an extra resonance appears, due to xenon condensation on the particles' external surface that competes with sorption within the micropores. Below 205 K the chemical shift of the confined xenon remains virtually unchanged. The easy accessibility of the galleries created by the ammonium pillars was demonstrated by the fact that the signal of the confined xenon was recorded in less than 200 ms after the flow of hyperpolarized Xe was put into contact with the sample. In addition, the lipophilic nature of xenon allows favourable interactions with organic TEA even in the extreme dilution of 1.25% of the gas mixture.

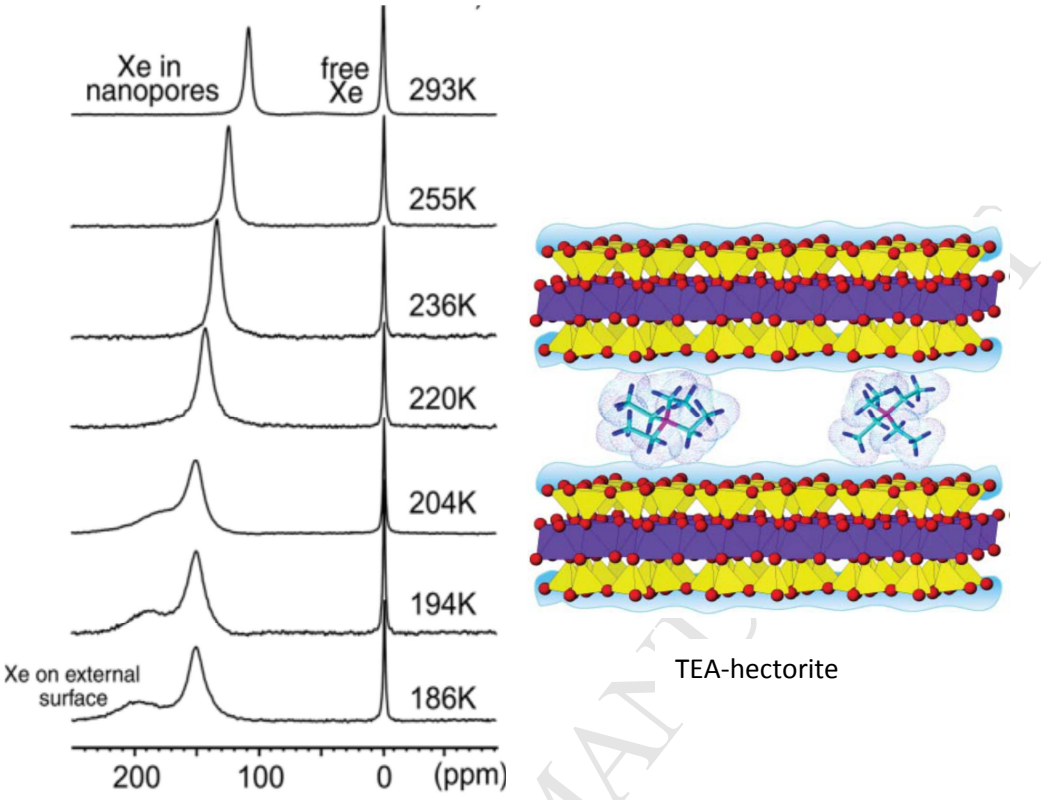

Figure 8. ^{129}Xe NMR spectra of xenon diffusing in the interpillar structure of TEA-hectorite at variable temperature. From reference [122] with permission.

The famous pre-Columbian Maya Blue (MB) pigment has been the subject of several publications [123–125]. Most research focused on explaining the extreme stability of this hybrid organic/inorganic pigment, which is present in mural paintings in Mayan ceremonial sites in the Yucatan, as well as in many ceramic pieces. The MB pigment consists of fibrous palygorskite clay hosted indigo molecules. Palygorskite is a phyllosilicate whose pore structure can be seen as unidimensional channels with 3.7×6.4 Å cross-section. Indigo is an organic dye, $C_{16}H_{10}N_2O_2$ (4.8 to 12.3 Å in size) with a quasi planar structure. Nowadays, the Maya Blue is prepared from synthetic indigo whereas the traditional method used a plant containing the indigo pigments. It appears that the synthetic Maya blue has not the same stability as the traditional one. In

order to elucidate the reason of such different behaviour, Maya Blues prepared according to the two methods and subsequently aging or not, acid treated or not, have been investigated by ^{129}Xe NMR, among other techniques [126]. When plotting the chemical shift of ^{129}Xe adsorbed in the different samples versus the pigment content (Figure 9), it appears clearly that the synthetic MB is similar to the palygorskite clay itself while the traditional MB shows higher chemical shift and a curvature at low loading typical of the presence of strong adsorption sites. This observation proves that indigo pigments are located in the palygorskite porosity for the traditional MB while they remain on the external surface in the synthetic MB. The authors explain this result involving the presence in the plant of indoxyl, a precursor of indigo, which is a smaller molecule and can diffuse inside the clay and is subsequently oxidized and transformed to indigo during aging.

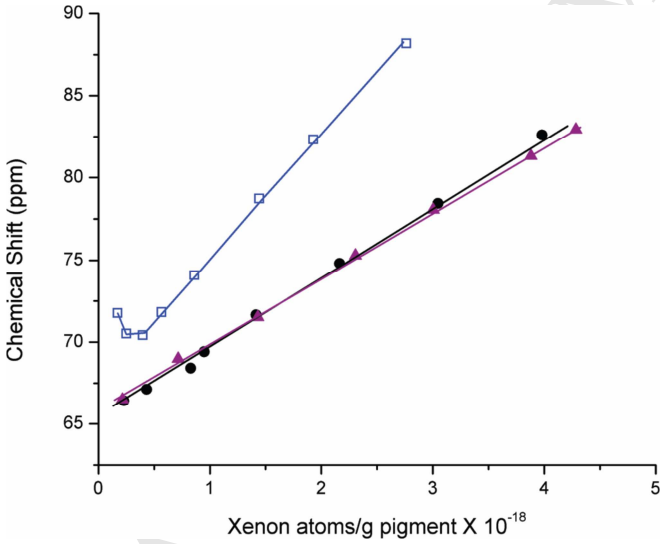

Figure 9. ^{129}Xe chemical shift as a function of concentration of xenon in samples after acid treatment. (▲) palygorskite, (□) traditional MB and (●) synthetic MB. From reference [126] with permission.

4.8. Other microporous solids

The group of Ripmeester has used and developped ^{129}Xe NMR extensively since the 80s. In particular, they studied thoroughly the class of hydrate (or more generally clathrate) materials and published numerous interesting papers. Owing to the formation of hydrogen bonds between the molecules, clathrates/hydrates form host materials that do not exist without guest molecules. Xe atoms are able to form hydrates or clathrates which can accommodate one or several Xe atoms [127]. In the last years, they could perform double quantum NMR experiments in order to distinguish single from multiply-occupied cavities of solid-state inclusion compounds based on dianins [128]. To detect the occupancy of cavities presenting several (usually two) adsorptions sites, they take advantage of the homonuclear ^{129}Xe-^{129}Xe dipole-dipole coupling that may exist between two Xe atoms in close spatial proximity. Indeed, it is possible to exploit this coupling to create a "Double Quantum (DP) coherence" that can be detected by NMR spectroscopy using an appropriate DQ dipolar recoupling pulse sequence under MAS conditions. The ^{129}Xe nuclei are previously decoupled from ^{1}H nuclei of the surrounding organic environment. Then, the signals in the DQ filter ^{129}Xe CP MAS spectra arise from ^{129}Xe nuclei which undergo dipole-dipole coupling inside the cavities (Figure 10).

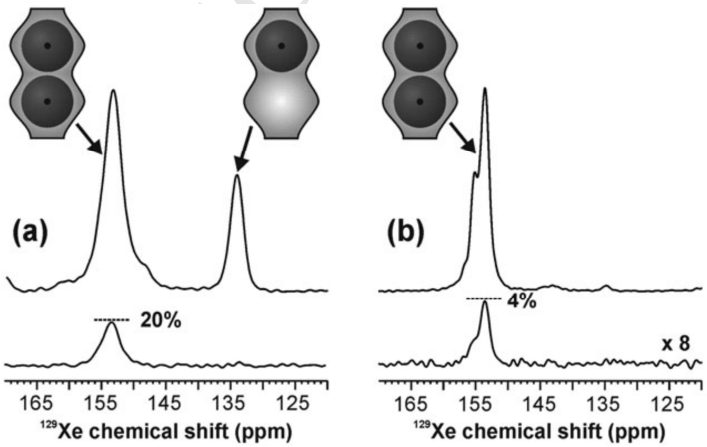

Figure 10. ^{129}Xe CP MAS (upper) and DQ filtered (lower) spectra for Dianin's compound prepared under (a) 1 atm of Xe gas enriched to 99% in ^{129}Xe and (b) 3 atm of Xe gas with natural abundance (26%) ^{129}Xe. The peaks are assigned to xenon atoms located in cavities containing either one or two xenon atoms based on the ^{129}Xe DQ filtered spectra. From reference [128] with permission.

Recently, in the aim of modifying structure and properties of clathrates, Shin *et al.* prepared clathrates hydrates by replacing water molecules with by NH_4F [129]. Xe NMR has revealed subtle structural modifications of clathrate cages upon the substitution of water molecules by NH_4F. The data analysis was supported by density functional theory calculations of the chemical shift.

In the aim of designing microporous materials that can facilitate the fabrication of monoliths which present better mechanical properties for industrial processes, the synthesis of a new type of microporous nanocomposites with catalytically active nickel nanoparticles has been reported by Zaheer *et al.* [130].

These authors synthesized a microporous composite from a commercially-available polysilazane chemically modified using a N-ligand stabilized nickel complex. The latter catalyzes the cross-linking of the polymer via hydrosilylation at room temperature. Upon pyrolysis at 600 °C under nitrogen, the generation of porosity and nickel nanoparticles is achieved. The surface area, the pore volume and the size of metal particles can be tuned by adjusting the amount of nickel complex. Monoliths, thermally stable up to 500 °C in an oxidative environment can be fabricated. The authors used HP ^{129}Xe NMR to probe the influence of specific thermal treatment and the quantity of Ni complex on the formation of microporous nanocomposites with catalytically active Ni particles. At moderate Ni contents, the paramagnetism of Ni particles induces a signal broadening but at higher Ni loading no signal is detectable due to HP Xe depolarization

and broadening. Thermodynamics of xenon adsorption was evaluated using the amount of the adsorbed and gas phase versus temperature obtained from the intensities of the respective signals in variable-temperature HP Xe spectra. Three regions are distinguishable (Figure 11). Only the linear segment of the Ln (I_{ads}/I_{gas}) = f(1/T) curve in the region of high temperature is used to extract pertinent thermodynamic parameters. The turning point at 255 K reflects a slower diffusion that limits the replacement of adsorbed Xe with freshly HP Xe.

The fast depolarization observed with Ni-100 composite is likely due to the high Ni content. Besides, for this compound, there is a substantial line broadening when temperature decreases due to paramagnetic effects of Ni particles more effective at low temperature.

In case of Ni-133 containing less Ni, the changes of slope in Ln (I_{ads}/I_{gas}) = f(1/T) is attributed to changes in the internal structural arrangement. Interestingly, an additional contribution to the single line observed at room temperature appears at each transition and is associated to some change within Xe exchange processes.

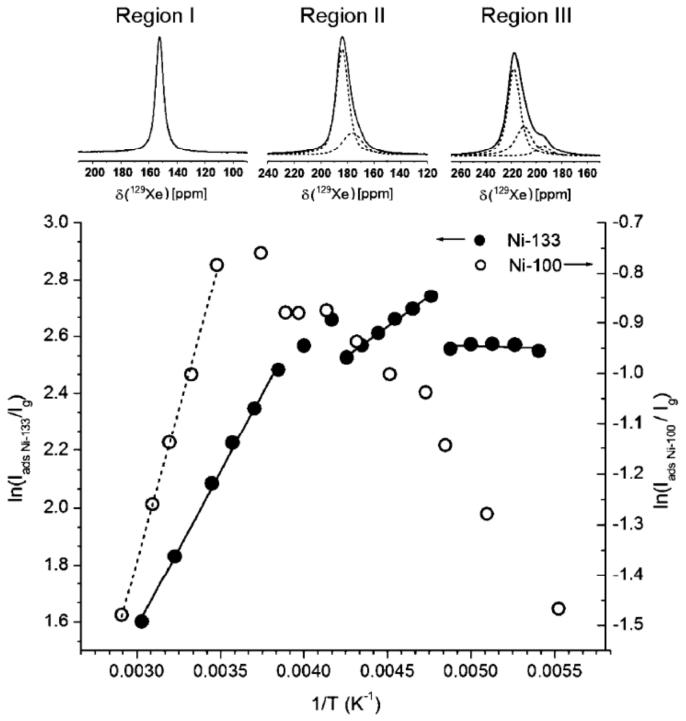

Figure 11. Natural logarithm of the integrated NMR signal intensity ratios, $I_{adsorbed}/I_{gas}$ for materials with Si/Ni = 100 (open symbols) and Si/Ni = 133 (full symbols). Region I, II, III correspond to temperature ranges of 333-235 K, 238-210 K, 212-180 K respectively. Inset: spectra of Ni-133 materials referring to the three regions. From reference [130] with permission.

5. Mesoporous solids: towards spectroscopic correlation "xenon-pore size"

It was observed that the relationship between the chemical shift (δ) and the pore size (D), established for zeolites at first, cannot be utilized for mesoporous silicas. Indeed, for similar pore sizes, the chemical shift is higher for xenon adsorbed in mesoporous silicas than in zeolites. Later, a new relationship has been proposed for mesoporous silicas by Terskikh *et al.* [55,89]. As for zeolites, the new hyperbolic relation has been also rationalized using a two-site fast exchange model (see section 2.2.).

5.1. Xenon adsorbed on mesoporous silica

Since 1991, great interest has been drawn to a new class of mesoporous silica materials, namely M41S. Most studies concerned the representative members of the family, i.e. MCM-41 [131] and SBA-15 [132] in powder or in thin films silica [133] and non-silicate oxide [134].

HP xenon NMR spectroscopy has been widely used to understand the structure of these mesoporous materials. It has been also confirmed to be a powerful tool to obtain fast and reliable information concerning the distribution of metal particles inside the porosity [135] or the internal structure of organically-modified mesoporous materials [136]. Valuable information regarding the presence of strong adsorption centres associated with modification of the chemical composition of the mesoporous materials and the presence of an interaction between xenon and the organic phase can be obtained. Structural properties as well as heats of adsorption are obtained by combining variable-pressure continuous-flow HP ^{129}Xe NMR measurements and the evolution of the ^{129}Xe NMR chemical shift.

For example, Zhang *et al.* studied the distribution of gallium nanocrystals in mesoporous MCM-41 using continuous-flow HP ^{129}Xe NMR spectroscopy [137]. They have shown that, in contrast to TEM, the laser-polarized ^{129}Xe probe can detect the whole region of the sample and provide the overall distribution of gallium in the MCM-41 host. With increasing gallium loadings, more and more gallium is introduced into the mesochannels of MCM-41 but a portion of gallium remains in the interparticle voids. There are still empty mesochannels left even at high gallium loading of 65.1 wt %, which indicates that the distribution of gallium nanocrystals in MCM-41 is heterogeneous. The adsorption heat evaluated from the variations of ^{129}Xe chemical

shift with the temperature reveals a physical adsorption of xenon in the Ga/MCM-41 meso-composites. This approach opens a sensitive way to probe the distribution of high content species in porous host materials.

Extensive use of variable pressure HP ^{129}Xe NMR allowed Galarneau *et al.* to better understand the processes of dissolution/redistribution of silica in MCM-41 and SBA-15 materials (synthesized at 60, 100 and 130 °C) under water treatment [138]. In general, the pressure dependence of xenon chemical shift in mesoporous materials contains information about the homogeneity of the pore surface/structure. The deviations from pressure-independent behaviour of the chemical shift (which is typical for uniform mesoporous structure without surface defects) reveals the presence of sites of preferential adsorption of xenon associated with the presence of micropores, whereas the sign of such deviation contains information about connectivity of micro- and mesopores. The results of the analysis of BET and ^{129}Xe NMR data allowed the authors to propose a schematic representation of the pores in SBA-15 materials, synthesized at different temperatures (Figure 12). Materials synthesized at 60 °C and 100 °C reveal the presence of microporous coronas around mesopores, whereas the synthesis temperature of 130 °C results in interconnected systems of mesopores without microporosity. These differences in structure lead to remarkably different behaviour under water treatment. Water treatment of MCM-41 even at very mild conditions leads to the formation of constrictions at the pore entrances evidenced by the change of the xenon chemical shift versus pressure dependence pattern. SBA-15 having micropores were shown to be surprisingly unstable in water although the material has much thicker walls than MCM-41. Only materials synthesized at temperatures exceeding 100 °C avoid heavy restructuration upon water treatment.

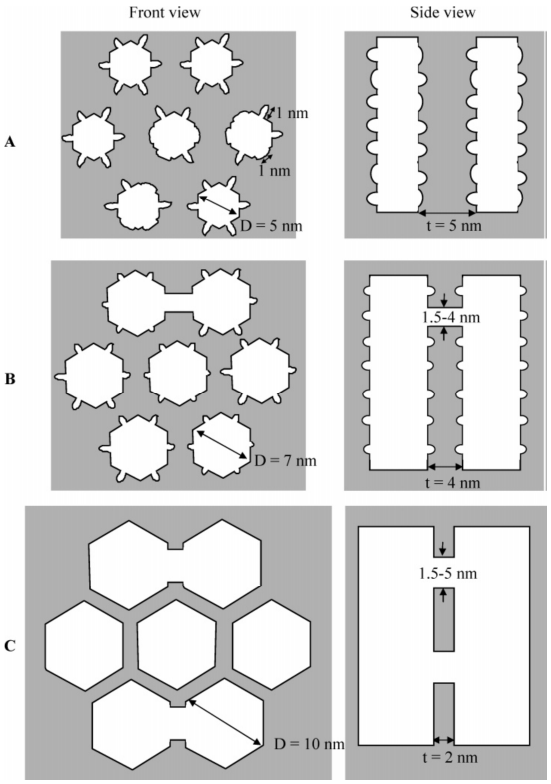

Figure 12. Schematic representation of three SBA-15s synthesized at (A) 60, (B) 100 and (C) 130 °C, revealing different pore diameters, wall thicknesses, microporosities and interconnections between main channels. From reference [138] with permission.

5.2. Porosity measurement of alumina catalysts

Recently, we explored the complex porosity of transition aluminas with ^{129}Xe NMR [139]. In these aluminas the porosity is generated by the aggregation of non-porous crystalline platelets (about 2-20 nm in size). The aggregates themselves (30-500 nm) form agglomerates (5 μm-10 μm). Finally, the alumina powder is compressed to produce extrudates (mm size) for industrial catalysis applications. Then, the porosity is the sum of the inter-particle spaces at various scales [140].

It was shown that the relationship δ-D is not suitable for aluminas, the chemical shift of xenon adsorbed in aluminas being higher than that adsorbed in silica for the same pore size. A new relationship was derived for aluminas [139]. The chemical shift has been

expressed as a function of volume-to-surface (V/S) ratio, determined by nitrogen adsorption measurements, rather than of pore size to avoid any hypothesis on the pore geometry. Indeed, due to the origin of the porosity, the pore shape cannot be described by a simple geometric figure. On the other hand, it was necessary to determine optimal experimental conditions in order that the chemical shift depends on the pore size only. In particular, the temperature of the thermal treatment for outgassing samples has a great influence on the nature of the crystallite surface, i.e. the type and number of Lewis sites formed when the surface is dehydrated/dehydroxylated. These sites constitute strong adsorption sites for xenon leading to an increase in the chemical shift at low pressure. To minimize the influence of these sites on the chemical shift, the samples were evacuated at rather low temperature (300 °C) and the NMR measurements were performed at pressures about one atmosphere.

Figure 13 compares the relationship recently established for aluminas to that of silica gels and mesostructured silicas (MCM-41, SBA-15).

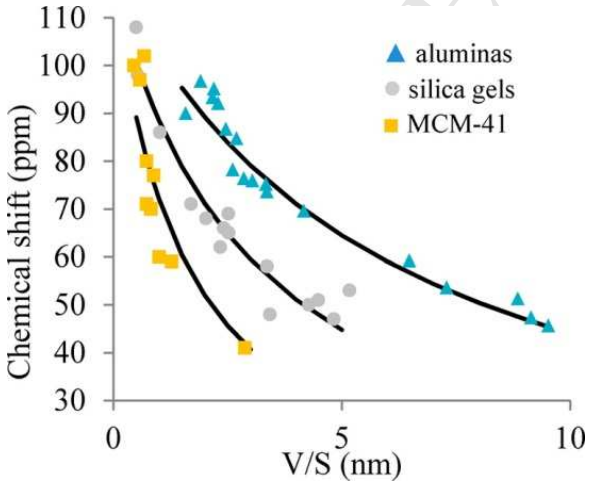

Figure 13. ^{129}Xe NMR chemical shift versus V/S ratio for aluminas, silica gels and MCM-41. The lines are the nonlinear least-squares fits of the data with equation 2 (section 2.2). From reference [139] with permission.

The fits of the chemical shift variations versus V/S with equation 2 (see section 2.2), give similar values of δ_a (characterizing the Xe-surface interaction, see section 2.2) showing that the Xe-surface interaction does not differ much for all these oxides. The difference between the curves is then reflected in the values of the adsorption constants, K_{ads}, obtained from the fits. It has been observed that these values are substantially smaller than the K_{ads} values determined from xenon adsorption isotherms. It was then proposed that the difference originates from the V/S values chosen as abscissae. The NMR experiments being performed at high pressure the measured chemical shift comes from Xe atoms diffusing in a restricted mesopore volume. The very small voids formed at contact between platelets are filled with Xe atoms, responsible of the higher chemical shift observed at low pressure but negligible at high pressure (Figure 14). Therefore, the V/S ratio corresponding to the pore volume sampled by the Xe atoms should be greater than the V/S ratio calculated from nitrogen adsorption.

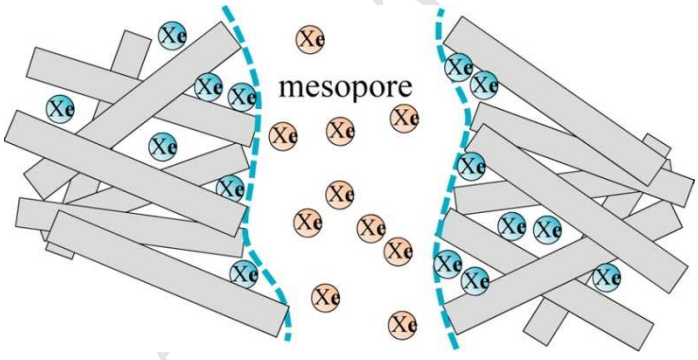

Figure 14. Schematic representation of the apparent surface (dotted blue line) accessible to Xe atoms diffusing in the mesopores. From reference [139] with permission.

γ-alumina is the usual support of the catalysts used for the hydrodesulfurization of petroleum fractions as diesel and kerosene. The alumina extrudates are impregnated by molybdenum containing solutions to deposit Mo phase eventually promoted by cobalt or nickel. During the catalytic process the Mo phase forms MoS_2 crystallites [141]. The group of Hagiwara studied sulfided Mo/Al_2O_3 [142] and $Co\text{-}Mo/Al_2O_3$ [143,144] catalysts by ^{129}Xe NMR. The metallic phase acts as strong adsorption sites for xenon adsorption and the chemical shift variations versus the xenon loading (N) show the typical deviation at low N. δ increases with the Mo content (by more than 50 ppm for 20% Mo) as well as, for a given Mo content, with the sulfurization temperature (by about 35 ppm between 373 to 773 K). The authors correlate the increase in δ to the coordinatively unsaturated sites on the edge of MoS_2 crystallites that are increasingly formed with the sulfurization temperature [142].

For Co-doped Mo/Al_2O_3 catalysts, before sulfidation, the signals are broader and shifted with respect to non-doped catalysts due to the paramagnetic effect of cobalt oxides such as $CoAl_2O_4$ and CoO. The paramagnetic effect is reduced after sulfidation owing to the transformation of these oxides into antiferromagnetic sulfides (Co-Mo-S phase). Nevertheless the magnetic effect increases with the Co/Mo ratio but it reaches a maximum for $Co/Mo \geq 0.7$ mol/mol. It slightly decreases for higher Co content because of the formation of diamagnetic Co_9S_8 at the expense of the Co-Mo-S phase [144].

5.3. Xenon porometry

a) Typical xenon porometry spectra

Generally, due to the fast diffusion of the adsorbed xenon, the ^{129}Xe NMR signal reflects an average of large amount of pores sampled by the atoms during the time scale of the NMR measurement. To overcome this difficulty the group of Jokisaari proposed

a novel method, named “xenon porometry”, for the characterization of porous solids [145–149]. In this method, the porous materials are immersed in a medium which can be liquid or solid at temperatures of measurements in order to ensure a slow diffusion of the xenon gas. It has been observed that, in such conditions, the chemical shift of the signal arising from the Xe atoms trapped inside small cavities formed in the pores when the medium freezes is highly sensitive to the local pore size [147].

Xenon porometry has been applied to probe the mean pore size and pore size distribution of different types of controlled pore glasses (CPG). A nice example has been given by Telkki *et al.* for CPG-81 (with average pore diameter of 81 Å), immersed in naphthalene [149]. Figure 15 shows that the xenon spectra which contain several peaks can be divided into three classes according to the melting temperature, T_{mp}, of the medium.

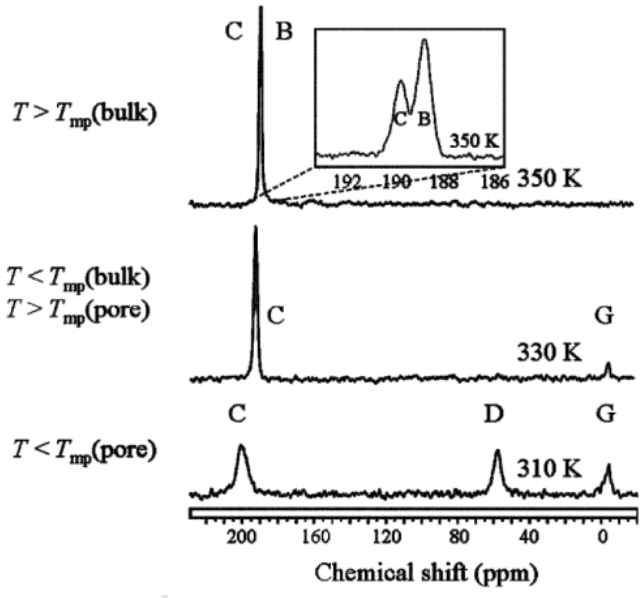

Figure 15. Typical xenon porometry spectra observed for CPG-81, containing Xe and naphthalene, in the different temperature ranges determined by the melting points of the medium. From reference [149] with permission.

For $T>T_{mp\ (bulk)}$, naphtalene is liquid. One can observe two close signals B and C arising from xenon dissolved in naphtalene between the particles (bulk liquid) and inside the pores, respectively. For $T=T_{mp\ (bulk)}$, the bulk medium becomes solid leading to the disappearance of signal B. At lower temperatures ($T<T_{mp\ (pore)}$) naphtalene situated inside the pores becomes solid. Then, a new signal, D, appears during the freezing process. This peak has been attributed to xenon atoms in very small cavities or pockets formed inside the pores during the freezing of the confined naphtalene [145]. The chemical shift value of signal D can directly be related to the pore size of the material.

b) Pore size distribution

Xenon porometry is suitable for the determination of pore size distributions of porous materials since the NMR signals of all the xenon atoms confined in the different parts of the sample represent the pore size distribution.

For CPG-81, Telkki *et al*. have shown, by 2D EXSY, that the xenon exchange between the pores corresponding to C and D signals is sufficiently slow so that the chemical shift of a xenon atom is characteristic to one pore size [149].

In conclusion, information about pore size and pore size distribution can be obtained by performing a series of ^{129}Xe NMR spectra for a wide domain of temperature. Figure 16 illustrates the different aspects of “xenon porometry” to determine the pore size. By converting the chemical shift scale of the spectrum into a pore radius scale, the pore size distribution can be obtained.

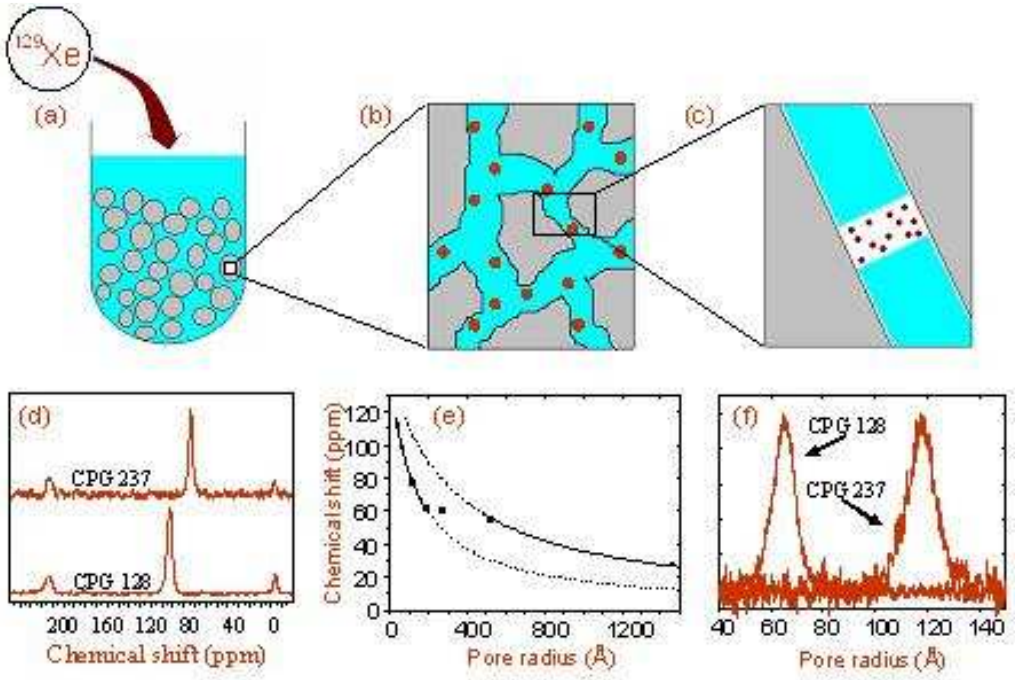

Figure 16. Determination of pore size distribution by xenon porometry using a solid medium. The porous material is immersed in a liquid medium, and xenon gas is added to the sample (a). Dissolved xenon atoms (dots) diffuse inside the pores (b). During freezing, empty pockets build up in the pores due to contraction of the medium and xenon squeezes out from the solidifying medium into the pockets (c). The chemical shift of xenon inside the pocket depends on the pore size, and the distribution of the signals observed from the different pores represents the pore size distribution (d). Using the determined correlation (e), the pore size distribution can be obtained by converting the chemical shifts to pore radii (f). From reference [150] with permission.

6. Hierarchical solids

Due to their well-defined micropores sizes for molecular shape selectivity, large specific areas, intrinsic acidity, zeolite-type materials have shown a great number of applications in many modern industrial processes related to catalysis, adsorption and separation. However, the limited diffusion of relatively large molecules in zeolite micropores often results in a poor access of reactants to the active sites, a blocking of the diffusion path and finally a fast deactivation of the zeolites.

To solve the diffusion difficulty of large guest species and to combine the advantages of microporous zeolites having high catalytic activity and stability with mesoporous materials presenting large pore sizes, a class of hierarchical materials has emerged at the beginning of the 2000s. Different strategies have been investigated: creating mesopores within zeolite crystals, coating the walls of mesoporous materials with zeolite nanocrystals, synthesizing zeolite crystals around templates organized in micelles with the goal of obtaining interconnected micro and mesopores. The characterization of the porosity is usually performed by N_2 adsorption or high resolution transmission microscopy. The first technique implies models that are not always realistic and the second is not easy due to the sensitivity of zeolites to the electron beam. In this context, ^{129}Xe NMR appears to be useful to obtain information on the pore structures of the composite materials and many papers have been published on this subject.

Due to the great interest of ZSM-5 zeolite, several studies concern ZSM-5-based hierarchical materials. When the starting material is the mesoporous silica solid and the zeolite is subsequently formed in the mesopores, detecting the presence of the zeolite nanocrystals is of great interest. Usually, X-ray diffraction cannot be used due to the small size of crystals and the sensitivity of ^{129}Xe NMR, especially with HP Xe, is therefore very useful. Examples are given here after.

Habib *et al.* have chosen to partially transform the amorphous walls of mesoporous Al-SBA-15 silica into ZSM-5 zeolite under hydrothermal conditions [151]. They investigated the influence of different parameters, such as the quantities of ammonium chloride and ZSM-5 template (TPABr) with the assistance [152] or not of microwaves [151,153]. When XRD patterns do not show diffraction peaks, the presence of ZSM-5

zeolite can be detected by a corresponding signal in the ^{129}Xe spectra as shown in Figure 17.

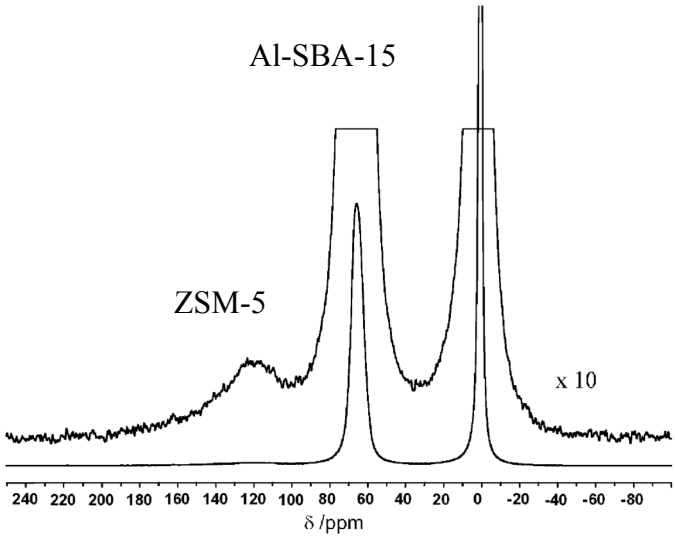

Figure 17. HP ^{129}Xe NMR spectrum of ZSM-5/Al-SBA-15 composite obtained by partial conversion of the walls of Al-SBA-15 into ZSM-5 zeolite. From reference [151] with permission.

Depending on the synthesis conditions of these composite materials, one can obtain only one line at low xenon pressure. The signal splits into two lines as pressure increases. This is the sign of a close proximity of the micro and mesopores since the Xe atoms can exchange rapidly, at low xenon loading, between the two environments giving rise to a coalescence signal. As pressure increases, the amount adsorbed in the zeolite crystals increases, reducing the diffusivity of Xe atoms and therefore the exchange. Then, the two environments become distinguishable, the chemical shift of the two signals tending to that of pure ZSM-5 and pure SBA-15 as pressure increases (Figure 18).

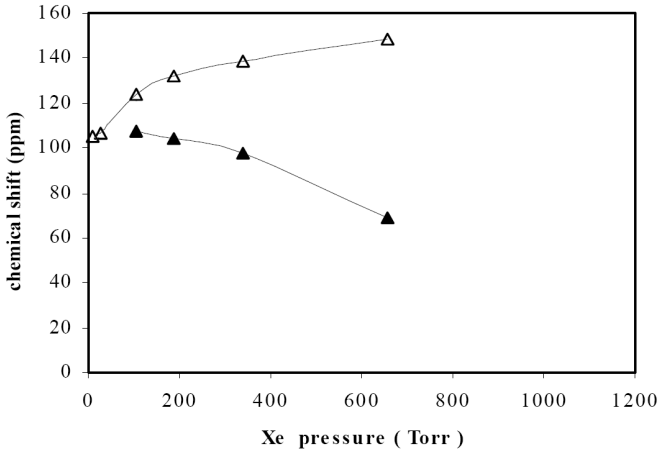

Figure 18. Chemical shift versus Xe pressure of Xe adsorbed in ZSM-5/SBA-15. Adapted from reference [153] with permission.

At low Xe pressure, the "decoalescence" of the single line can also be obtained when decreasing the temperature as shown by Liu *et al.* in mesopore-modified ZSM-5 zeolites synthetized in presence of starch [154].

Generally, the presence of two signals corresponding to the micropores (zeolite) and the mesopores (SBA-15) does not give any information on the connectivity of the two types of pores. In this case, one can use 2D EXSY experiments to explore the pore connectivity. The comparison of the 2D spectra of the composite materials with those of a mechanical mixture of ZSM-5 and silica is helpful to conclude to the interconnectivity the pores.

When the walls of the starting mesoporous materials are completely transformed into zeolite structure, it appears to be impossible to observe two lines, even at low temperature (down to 143 K). It is the case of multimodal Zr-silicalite-1 nanocrystals aggregates obtained from a meso-macroporous zirconosilicate with amorphous structure which are transformed into MFI structure using TPA template in the presence of glycerine, the latter maintaining the porous hierarchy [155].

An interesting study is that of a mesoporous LTA zeolite. Cho *et al.* synthesized mesoporous NaA zeolites by adding organosilane surfactants and eventually triblock copolymers as pore expanding agents [156]. They obtained mesoporous NaA zeolite presenting mesopores from 6 to 10 nm (up to 24 nm with expanding agents). The NMR spectra of xenon adsorbed in these mesoporous zeolites are characteristic of NaA, as mentioned above. They show several lines corresponding to the different Xe populations inside the α-cavities, since the Xe atoms do not exchange rapidly between the cavities [91]. There is an additional line at ca. 30 ppm due to Xe atoms adsorbed in the mesopores (Figure 19). The creation of mesopores inside the zeolite crystallites drastically increases the zeolitic external surface area allowing Xe atoms enter into the cavities situated near the surface. In mesoporous NaA, the fraction of such cavities is very large compared to that in parent NaA zeolite presenting cubic 2-3 μm crystals and enhances the amount of Xe adsorbed in the chosen conditions.

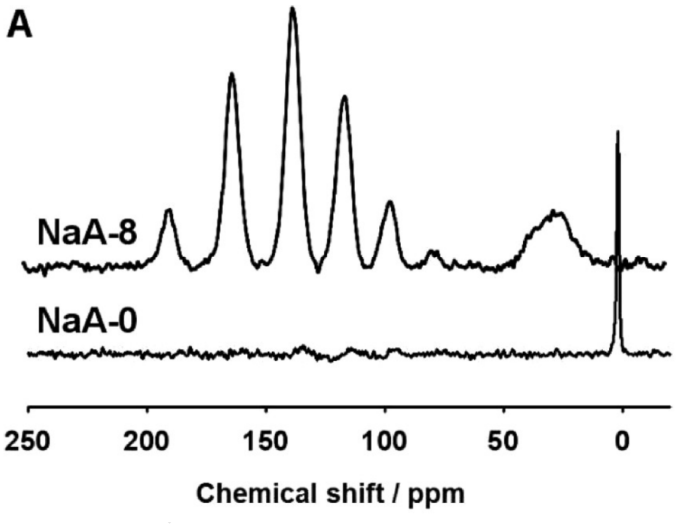

Figure 19. ^{129}Xe NMR spectra of hierarchical LTA zeolite (NaA-8) and conventional LTA zeolite (NaA-0). Each spectrum was accumulated for 1 d, after xenon contact for 12 h under 1.01×10^5 Pa at 297 K. From reference [156] with permission.

Analysing the kinetics of Xe adsorption on parent and mesoporous NaA zeolites using the Fick's law, the authors determined diffusion coefficients of Xe in these solids and were able to correlate the diffusion rate to the external surface area. The Xe atoms diffuse 200 times faster in mesoporous NaA than in purely microporous NaA. The effect of mesoporosity on the catalytic performance of these catalysts has been investigated in the conversion of methanol.

One can also start from a zeolite and destroy the structure partially to create mesopores within the crystals. This strategy was used by van Miltenburg *et al.* to obtain mesoporous MCM-22 zeolite [157]. Previous Xe NMR studies of MCM-22 zeolite (MWW) showed that the spectra consist of only one line while the structure presents two types of non-interconnected pores, oblate cavities connected to each other through six 10-ring windows forming layers and 2-dimensional sinusoidal interconnected 10-ring channels running within layers in between the cavity layers [104,158]. Some authors have attributed this line to the cavities solely [158]. But, examining the internal dimensions of the voids, some of us have deduced that the mean free path of a Xe atom is similar in the two types of pores and therefore the chemical shifts have close values [104]. At high Xe loading, Xe-Xe interactions increase differently within the two types of pores leading to different chemical shift and two lines can be detected.

In the study of van Miltenburg *et al.*, the parent MCM-22 zeolite is subjected to alkaline treatment at 323 K during 45 min using NaOH solution at various concentrations. The spectra of the different mesoporous MCM-22 present one or two lines and their interpretation is however not yet fully understood.

The case of zeolite intergrowths is also interesting. The synthesis of certain zeolites presenting close structures, such as FER, EMT, MEL etc. leads to the formation of

intergrowths. It appears that the combination of different structures may have better catalytic performances for certain reactions.

In the late 80s, ^{129}Xe NMR has been revealed to be useful to determine the composition of mordenite/ferrierite intergrowths which is not easy to obtain by XRD when the monocrystalline domains are small [159]. More recently, Liu *et al.* have synthesised cocrystallized MCM-49/ZSM-35 materials [160,161]. MCM-49 and ZSM-35 have MCM-22 (MWW) and ferrierite (FER) structures, respectively. Variable-temperature HP ^{129}Xe NMR experiments performed on the intergrowth (cocrystallized MCM-49/ZSM-35) and on a mechanical mixture of MCM-49 and ZSM-35 reveal that the Xe exchange between the two structures is faster in the cocrystallized sample because, at room temperature, the spectra of the two structures show signals at very close chemical shifts and only one line is observed. As temperature decreases, the signal broadens then splits into two lines at higher temperature for the mechanical mixture than for the cocrystallized MCM-49/ZSM-35 materials (Figure 20).

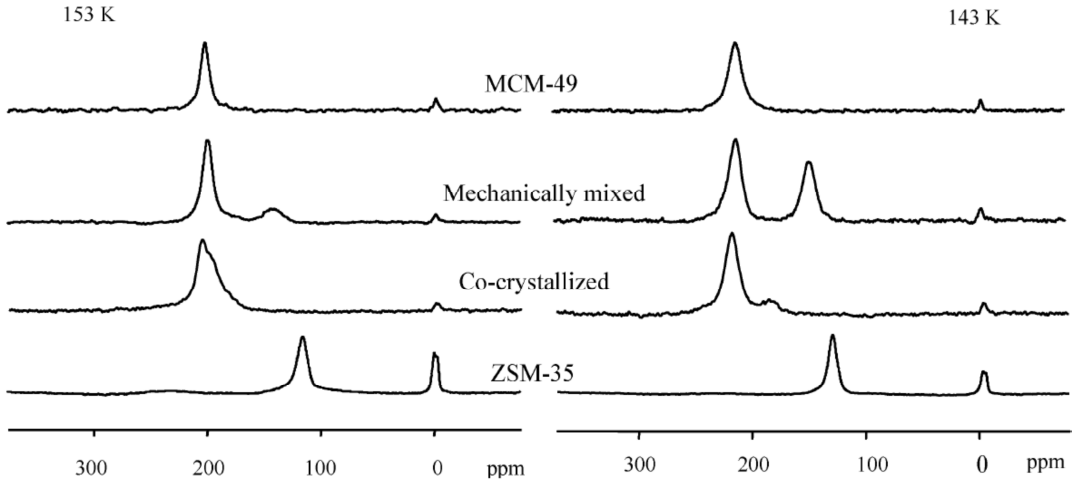

Figure 20. Hyperpolarized ^{129}Xe NMR spectra of Xe adsorbed in MCM-49, in mechanically mixed MCM-49/ZSM-35, in cocrystallized MCM-49/ZSM-35, and ZSM-35 zeolites at 153 and 143 K. From reference [160] with permission.

This conclusion was confirmed by 2D EXSY experiments performed on the cocrystallized and the mechanically mixed materials showing that Xe exchange between the different structures occurs at smaller mixing time for the cocrystallized sample.

7. Organic porous materials

7.1. Porous molecular crystals (PMC): permanent porous materials

PMC is a family of materials in which non-covalent bonds maintain robust architecture with a permanent porosity. In 1999 it was shown by Comotti *et al.* that crystals formed by van der Waals interactions between organic moieties can generate permanent porous materials [162]. Tris (*o*-phenylenedioxy) cyclotriphosphate (TPP) is recognized to be a the "zeolitic" organic material [163]. TPP absorbs guest atoms or molecules and when these latter are evacuated, the porous structure is retained. Continuous flow HP ^{129}Xe NMR was applied for the first time to investigate its open channel structure. Due to the Xe polarization enhancement by optical pumping, it was possible to follow the diffusion process of xenon in the TPP channels [164]. The spectra exhibit an anisotropic powder pattern signal because the Xe atom diameter is close to that of channels. Then, the chemical shift tensor reflects the Xe-wall interaction, Xe-Xe interactions being negligible at low pressure. These latter are not negligible at high pressure as shown by Kobayashi *et al.* using thermally-polarized ^{129}Xe.

Microporous dipeptides, also known as organic zeolites or biozeolites, are examples of small-pore peptide nanotubes [165]. These peptides constitute an interesting materials family to get thermodynamic and molecular scale information following the pore filling as a function of temperature based on ^{129}Xe NMR spectroscopy.

Direct observation of atoms entering and exiting self-assembled L-alanyl-L-valine (AV) nanotubes has been facilitated by continuous-flow hyperpolarized ^{129}Xe 2D-EXSY

NMR at 263 K [166]. The mixing-time dependence of the diagonal- and cross-peak intensities was fitted to an analytical expression assuming a slow exchange between the gas phase and a surface exhibiting Langmuir adsorption. At each pressure, the rate of desorption from the channels was determined. Xenon Pulsed Field Gradient (PFG) NMR and hyperpolarized xenon spin tracer exchange NMR experiments were also applied on AV nanochannels. They pointed out the existence of single file diffusion dynamics [167].

7.2. Xenon adsorbed on single crystal structure

A nice example about o p-tert-butylcalix[4]-arene single crystals has been studied by Brouwer *et al.* [168]. The authors showed that such van der Waals solid without channels, can take up small guests such as xenon without losing long-range order. ^{129}Xe NMR spectra clearly indicate that significant structural changes occur in local order even at low levels of loading.

When xenon is adsorbed in pores presenting anisotropic environment~~,~~ with dimension of the order of the Xe atom (4.4 Å) and less than twice the xenon diameter, the resulting NMR shift is governed by the orientation of the pores with respect to the direction of the magnetic field. In the presence of a powder sample, it gives rise to well-known shapes of the signal related to the symmetry or the absence of symmetry of the environment [169–171]. When a single crystal is placed inside the NMR magnet, a single symmetric line is observed and its position depends on the orientation of the crystal as it has been shown in case of MFI monocrystals [62].

More recently, it has been illustrated by Comotti *et al.* in the example of nanoporous van der Waals single-crystal of tris-orthophenylenedioxycyclo-triphosphazene which can be grown to the size of a few millimetres [172]. The spectra of one single crystal,

recorded for different orientations of the c axis of the crystal exhibits a single line whose position varies by 31 ppm when the crystal is rotated from a 90° angle (Figure 21).

This technique opens up the possibility of describing the orientation of the cavities in confining systems.

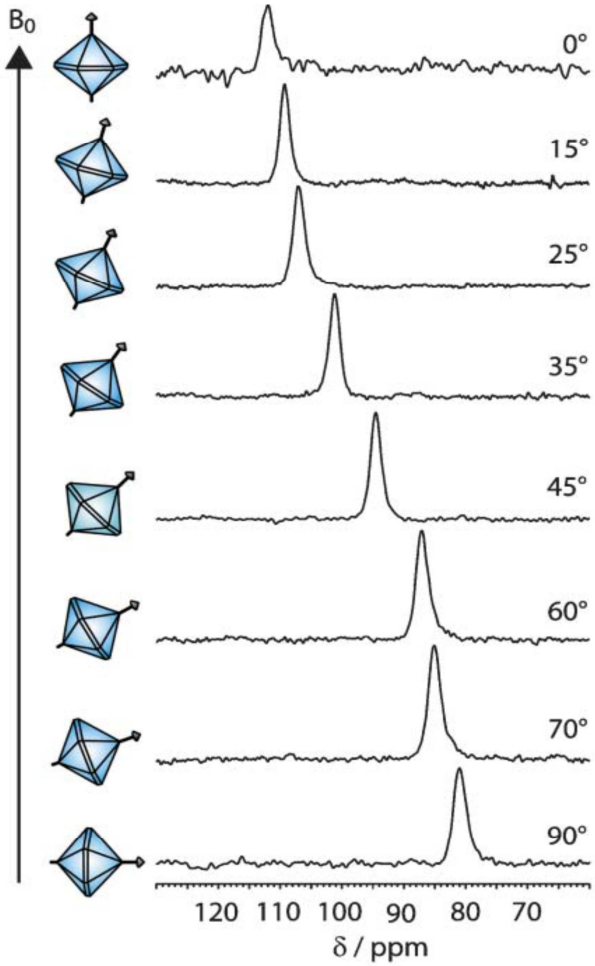

Figure 21. Continuous-flow hyperpolarized ^{129}Xe NMR spectra of the porous, molecular single-crystal inclined at different orientations θ from 0 to 90° with respect to the magnetic field B_0. From reference [172] with permission.

The coating of nanosize ZnO particles by organic silanes has been investigated by Kotecha *et al.* [173]. A ^{129}Xe NMR signal at high chemical shift (190 ppm) has been

attributed to Xe atoms entrapped in organic domains for high coverage rate. UV irradiation leads to the disappearance of the highly shifted line indicating a partial destruction of the organic phase accompanied by the formation of large pores.

7.3. Probing polymers by ^{129}Xe NMR

^{129}Xe NMR has been applied very early to polymers, in particular to study crosslinking, miscibility or porosity of polymers.

In the first papers, published in the 80s, it has been shown that xenon can adsorb in the amorphous part of polymers at temperatures below the glass transition (T_g) and it is also relatively soluble in rubber polymers.

As for microporous inorganic crystalline materials, xenon is used as a probe to evaluate the size of the microvoids existing in polymers. Weber *et al.* analysed the porosity of several polymers (specific surface area, pore size and pore volume) by adsorption experiments of different gas (N_2, Ar, CO_2) using various models and compared the results to that obtained with ^{129}Xe NMR [174]. The latter give average pore sizes in good agreement with those obtained by gas adsorption.

A direct application is found in the study of helical poly(phenylacethylene) which presents two helix forms: a stretched (cis-transoid) and a contracted (cis-cisoid) helix [175]. Depending on the helix form, three distinct polymers of different colours, noted Y (yellow), R (red) and B (black), obtained by different hexagonal arrangements of the chains present voids from 4.6 to 12.1 Å (Figure 22). One form of polymers can be converted to another when being in contact with acetylacetone solvent or exposed to $CHCl_3$ vapor. The ^{129}Xe NMR spectra of Xe adsorbed in the different forms of polymers show lines whose chemical shifts correspond to sizes consistent with those obtained by WAXS patterns and by simulation.

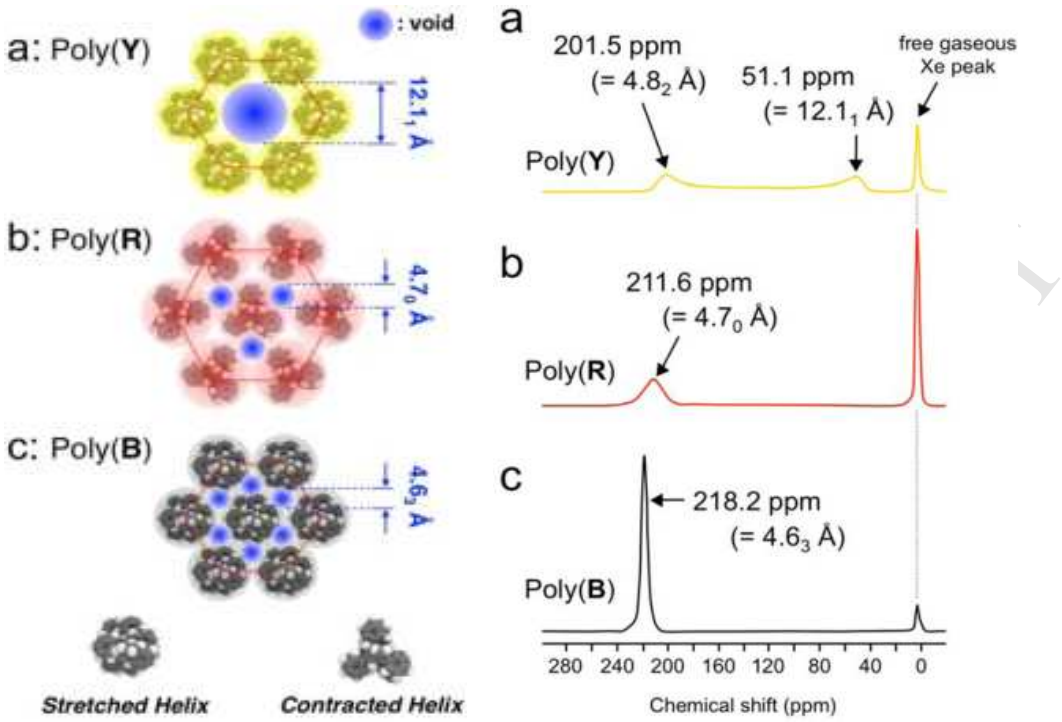

Figure 22. Top views of polymer columnars (left) and ^{129}Xe NMR spectra (right) of (a) Poly(**Y**), (b) Poly(**R**), and (c) Poly(**B**) at room temperature. From reference [175] with permission.

Another interesting application is found in the work published by Demco *et al.* who found a correlation between the chemical shift and the line width of the signal of adsorbed Xe with the Young modulus of drawn gel-spun ultrahigh-molecular weight polyethylene fibers. In particular, these authors showed that the average void diameter is an increasing function of the modulus [176].

Generally, the chemical shift is specific of a given polymer. Therefore, it can be used to follow phase separation as well as to measure domain sizes in multiphase blends. An example is given in a study of polypropylene (PP) and ethylene-propylene copolymer (EPR) particles of millimetre size with HP ^{129}Xe [177]. The PP and EPR domains give rise to signals characteristic of each polymer/copolymer and the intensities have been

measured as a function of temperature. Because HP ^{129}Xe was used, the intensities decrease with temperature and vanish at temperature corresponding to T_g, because the freshly hyperpolarized Xe cannot diffuse appreciably into the amorphous polymers. Since there is no coalescence of the signals, the average domain size has been evaluated at more than 200 nm taking into account diffusion consideration. 2D EXSY experiments were performed to better understand diffusion phenomena. In particular, it was concluded that the Xe atoms can enter the EPR phase and then diffuses in the PP one, but the reverse path is much less probable.

Due to the great sensitivity of HP ^{129}Xe NMR, the technique was successfully used to monitor mini-emulsion of styrene with high time resolution [178]. The chemical shift has shown to be linearly dependent on the molar fraction of monomer/polymer mixtures and allows determining the conversion rate as a function of time during the polymerization. The results are in good agreement with those obtained by calorimetry (Figure 23).

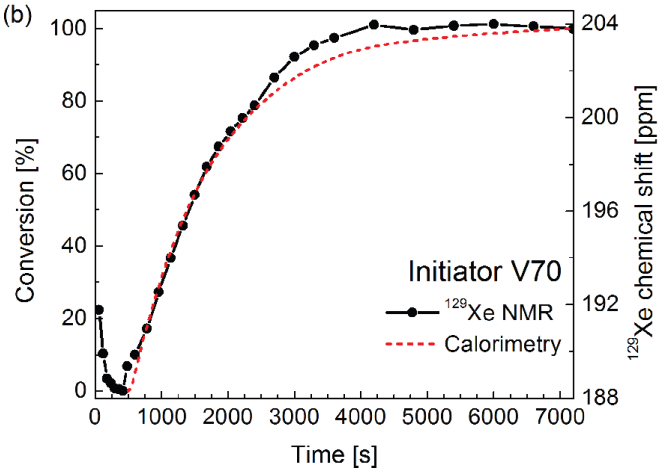

Figure 23. Comparison between ^{129}Xe NMR data (black solid line, the points show the chemical shifts) and calorimetry data (red dotted line). From reference [178] with permission.

Owing to the simplicity of the spectra and the simple relationship of ^{129}Xe chemical shift on the composition of reaction mixture, HP ^{129}Xe NMR is an excellent alternative to ^{1}H and ^{13}C-NMR (which exhibits complicated spectra) for investigating polymerization. In addition, the application of HP ^{129}Xe NMR spectroscopy for online monitoring of copolymerization reactions allowed following the conversion of each monomer independently as well as thermoneutral reactions which cannot be done by calorimetry.

Temperature-responsive hydrogels are a sub class of cross-linked polymers whose solubility behaviour as a function of temperature is governed by competing hydrophobic and hydrophilic properties. Above a critical temperature of the solution, the polymers become insoluble, the polymer matrices collapse and the solvent is expelled [179]. This interesting behaviour can be exploited for drug delivery. Poly(N-isopropylacrylamide) crosslinked with N,N'-methylenebis (acrylamide) shows this property and the degree of swelling, depending on the amount of crosslinker, has been followed by HP ^{129}Xe NMR [180]. The chemical shift is correlated to the degree of swelling via a bi-exponential relationship. It was possible to differentiate hydrogels, crosslinker concentrations and to define an optimal swelling for which all the solvent molecules are confined in the pores of the gel. This information is important for the goal of transporting the desired amount of drug to its target in an organism. Moreover, it has been shown that it is possible to monitor solvent uptake in real time due to excellent signal-to-noise ratio.

As for zeolites, the chemical shift increases with Xe pressure due to Xe-Xe interactions inside the microvoids of polymers and it is useful to measure the chemical shift versus pressure in order to determine the chemical shift at zero coverage, only due to the interaction between Xe and the polymer, which correlates with the pore size

[174,181,182]. One should be aware that the observed chemical shift may be the result of an exchange between dissolved and adsorbed Xe atoms, as in the case of polyphenyleneoxide (PPO) [182] and the chemical shift of the purely adsorbed Xe has to be determined (Figure 24). The adsorption isotherms can be used because they present typical shape (Figure 25) which is analyzed with a dual-mode sorption model involving dissolved Xe (following a Henry law) and adsorbed Xe (following a Langmuir law).

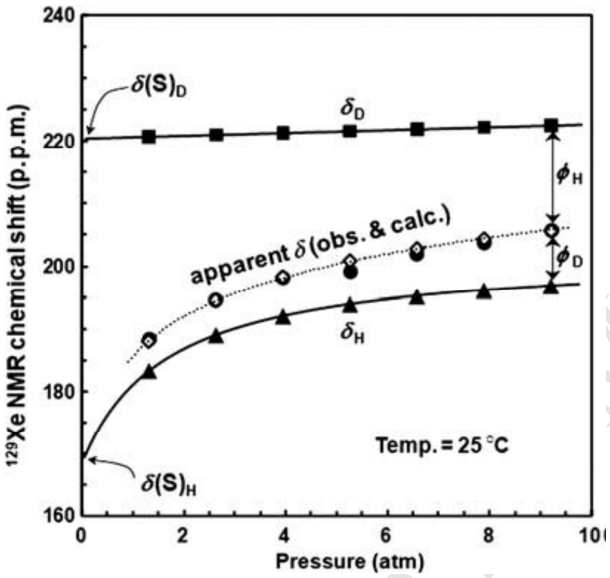

Figure 24. ^{129}Xe NMR chemical shifts of ^{129}Xe in PPO plotted against the Xe pressure at 25 °C. The symbols ◊,●,■ and ▲ are the observed δ, calculated δ and the δ_D (dissolved) and δ_H (adsorbed) components, respectively. From reference [182] with permission.

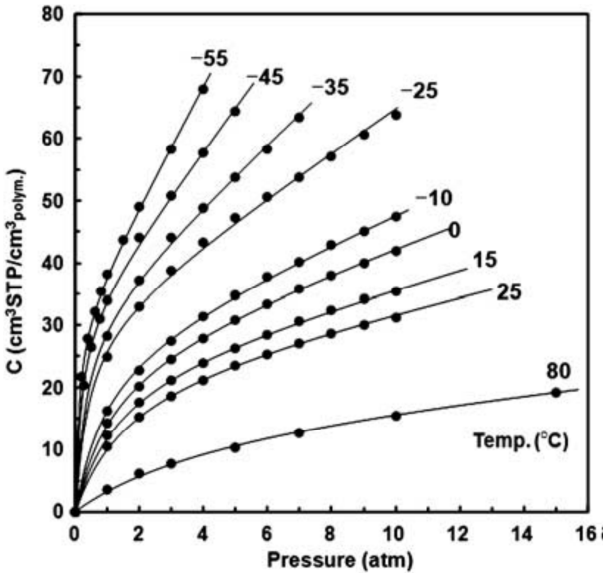

Figure 25. Xe sorption isotherms of PPO at various temperatures. The solid lines represent the nonlinear least-square curve fit using the dual-mode sorption model. From reference [182] with permission

The fit of the isotherms allows the determination of the adsorption constants and the respective concentrations of dissolved and adsorbed Xe and, therefore, the two components, δ_D (dissolved) and δ_H (adsorbed) of the chemical shift to finally obtain the true chemical shift of Xe adsorbed in the microvoids of the glassy polymer. A study as a function of temperature gives the variation of the size of the microvoids as temperature decreases below T_g.

A common method of synthesizing polymers is the emulsion polymerization. The determination of morphological characteristics of latex particles in dispersion is a key issue. To get a better picture of the particle structure in some polymer colloids, Locci *et al.* used ^{129}Xe NMR at 25 °C in combination with photon correlation spectroscopy which gives the hydrodynamic particle size [183]. If T_g is much greater than 25 °C, as for polystyrene (T_g = 107 °C), spectra exhibit two lines, one corresponding to Xe atoms

out of the particle (i.e. in the solvent) and the other to Xe atoms in the particles, having a higher chemical shift and larger width. On the contrary, if T_g is much lower than 25 °C, as for poly(n-buthyl acrylate) (T_g = - 46°C), a single narrow line is only observed corresponding to an exchange between sorbed and free Xe. A thorough analysis of the chemical shifts, the linewidths and the intensities versus pressure gives information on the particle core, the partition between sorbed and free Xe atoms as well as the rate constant characterizing the kinetics of the penetration of Xe into the particles. The latter is sensitive to the nature of the latex.

Polymers can be associated to silica to form hybrid membranes for gas separation or fuel cell applications. One example is found in the comparison of hyperbranched and linear polyimide- silica membranes for gas permeation [184]. The authors studied the effect of the amount of silica and the form of the di or tri-amine monomers on some gas (CO_2, O_2, N_2, CH_4) permeability coefficients. For the hyperbranched polyimide they observed a remarkable increase in the CO_2/CH_4 selectivity with increasing silica content. However, the ^{129}Xe NMR spectra do not show difference between the pure polymer and the hybrid (polymer/silica) membranes contrary to the case of linear-type polyimides. It was suggested that the cavities are not created in porous silica domains but around polymer-silica interface and the particular characteristic size, distribution, and interconnectivity of the cavities for the hyperbranched polyimide- silica hybrids lead to the remarkable CO_2/CH_4 separation ability.

In the case of poly(perfluorosulfonic acid)/silica composite used as proton exchange membrane for fuel cell applications, the free volume has been investigated by Utiu *et al.* [185]. These authors showed that the average size of free volume increases with the

silica content and reaches a maximum value at 2% of silica. This observation could be correlated to the performance of composite proton exchange membranes.

8. Hybrid porous materials

8.1. Multifunctional mesoporous silica materials

Among various mesostructures, organic/inorganic hybrid silica materials are especially exciting and promising for a wide range of applications in the fields of adsorption, chemical sensing, biology, and catalysis. For mesoporous silica, the relaxation times are particularly long and the signal of thermally polarized ^{129}Xe is generally very weak. The laser-polarizezd ^{129}Xe NMR has turned to be very useful to probe the pore structure and surface heterogeneity of materials with different porosities and chemical composition. In 2002, Moudrakovski *et al.* reported the first application of continuous flow HP ^{129}Xe NMR to study the structure of functionalized ordered mesoporous silica [186]. Huang *et al.* performed an extensive variable-temperature HP ^{129}Xe NMR study of a series of multifunctional mesoporous silica materials, prepared by introducing two different organoalkoxysilanes, during the base-catalyzed condensation of tetraethoxysilane (TEOS) [187]. Xenon NMR chemical shift was found to be sensitive to both the nature of functionalizing material and the degree of functionalization. It was observed, that the silanes anchored with shorter organic chains tend to interact with the surface silanol groups causing backbone bending and hence formation of secondary pores in the organic matter, as indicated by additional shoulder peak at lower field in the room-temperature ^{129}Xe NMR spectrum. It was also found that subsequent removal of functional moieties by calcination treatment tends to result in a more severe surface roughness of the pore walls in bifunctional samples compared to monofunctional ones.

Another series of silylated MCM-41 materials studied by Huang *et al.* revealed a good correlation of the observed ^{129}Xe NMR chemical shifts with both the surface coverage and the chain length of the grafted alkylsilanes ($H_3(CH_2)_{n-1}SiCl_3$, n = 1, 4, 8, and 12) [188]. The authors proposed a simple empirical relation in terms of the surface coverage, ρ, and the length of alkyl chain, n : $\delta_s = 105.4 + \rho\,(2.35 + 2.96n)$. The ratio of the deshielding medium contributions of methylene and methyl groups (2.96/2.35=1.26) determined by the authors deviates from this found for xenon dissolved in linear silanes (1.79). This difference was rationalized in terms of deshielding of the Si-CH_2 groups and/or the bulk magnetic susceptibility effect. Gédéon and coworkers studied SBA-15 materials functionalized with different arenesulfonic organic contents [136]. Variable-pressure data allowed the authors to better understand the distribution of organic groups in the pores of SBA-15. The introduction of organic groups onto the pore walls of the mesoporous silica leads to an increase in the chemical shift due to the smaller dimensions of the pores. At high organic content xenon atoms contact exclusively with organic moieties, and the modified mesoporous surface appears to be homogeneous from the NMR point of view, whereas for the highest grafting ratio the organic phase could completely block the entry of the Xe atoms in the mesopores. Nonlinear least-squares fitting of the chemical shift variation with temperature allowed the authors to determine the optimized values of the heat of adsorption, the adsorption constant and the characteristic chemical shift of xenon adsorbed on the surface, δ_a. The adsorption enthalpy is not noticeably affected by the functionalization of the surface, in contrast to δ_a values which were found to increase with the organic content. From the linear variation of δ_a with the surface coverage ρ, a value of the intrinsic shielding due to intermolecular Xe-organic group

van der Waals interactions,-$\sigma_{org,}$ of 8.65 ppm nm^2 was obtained for arenesulfonic functionalized samples.

The authors also performed polarization transfer (CP) experiments from HP ^{129}Xe to the protons of organic surface groups. The results of CP experiments show that only the alkyl protons are affected by the xenon polarization transfer. Indeed at 200 K, the residence time of xenon on the surface is quite long and the transfer originates mainly from these adsorbed atoms. Since the alkyl groups are closer to the surface, their signal is preferentially enhanced in the CP experiments.

8.2. Metal Organic Framework Materials

Metal–organic frameworks (MOFs) represent a class of hybrid materials built from organic and inorganic building blocks. The bonds between organic and inorganic constituents are relatively strong, resulting in two- or three-dimensional network structures. In most cases, these networks exhibit micro- or mesopores. As example, Figure 26 shows the structure of different MOF materials. The very high surface areas of MOFs materials sometimes up to 6000 m^2/g, their tunable pore sizes (ranging from 0.5 to 3 nm) and the extraordinary degree of variability for both the organic and inorganic components of their structures, make these materials suitable for a variety of applications including gas storage, molecular sieving, heterogeneous catalysis, membranes, thin-film devices and biomedical imaging. In a recent review paper, Sutrisno *et al.* have shown that solid state NMR is a powerful technique to characterize metal–organic frameworks [189]. This technique is complementary to diffraction methods and can be used to study local structure, dynamics of organic linkers and to monitor the behaviour of guest species.

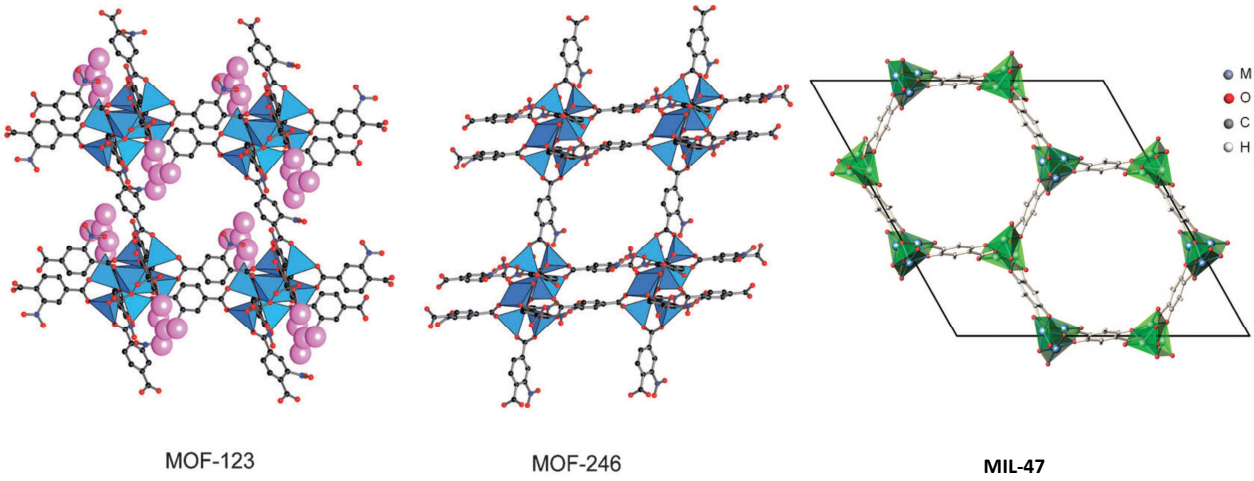

Figure 26. The framework structures of (A) MOF-123, (B) MIL-246 and (C) MOF-47. From references. [190,191] with permission.

The first application of ^{129}Xe NMR spectroscopy to MOFs was reported in 2006 by Boehlmann *et al.* [192]. In this study the porosity and the properties of the metal-organic framework $Cu_3(BTC)_2(H_2O)_3$ (BTC=benzene 1,3,5-tricarboxylate) were investigated. The results demonstrate that, depending on the synthesis pathway, either one or two signals are observed which can be attributed to xenon atoms adsorbed in two different pores. Co-adsorption experiments show that molecules such as ethylene and water totally block the smaller pores of the Cu_3-$(BTC)_2$ and therefore prevent the xenon atoms from penetrating these cavities.

The favorable properties of xenon adsorption and ^{129}Xe NMR have been later used in order to study the local structure of a $[M(II)_2(bza)_4(pyz)]n$ (bza and pyz = benzoate and pyrazine, M= Rh and Cu) metal-organic framework [193]. In this study, a 2D gas model (Fowler-Guggenheim equation) was used to analyze the isotherms, evaluating the xenon-xenon interaction and the isosteric heat of adsorption. The relatively large heat of adsorption (48 kJ/mol) is attributed to the strong Xe-π interaction. In case of Rh

complex, xenon adsorbed in nanochannels gives rise to an anisotropic and very de-shielded ^{129}Xe NMR resonance line. This phenomenon suggests that xenon atoms occupy sites with extremely small free volume. Single-crystal X-ray diffraction analysis revealed that rare gas atoms were accommodated in a one-dimensional (1D) nanochannel as a dimer Xe_2 structure. Furthermore, the temperature dependence of the ^{129}Xe chemical shift supports the results of X-ray diffraction and suggests that the Xe_2 dimer is the dominant local structure.

Porosity in solids composed of organic and metal-organic macrocycles has been investigated using HP Xenon NMR [194–196]. It was shown that the channel structure remains intact even upon removal of cocrystallized guest molecules. The first paper on organic macrocycle materials studied by xenon NMR has been published by J. Ooms *et al.* [195]. The ^{129}Xe NMR data provide information about the porous nature of the compounds for which X-ray crystallographic analysis was not possible. Data obtained from 2D EXSY experiments, variable-temperature ^{129}Xe NMR and molecular dynamics simulations suggest a mechanism whereby the xenon gains access to the highly confined sites via the channels.

The adsorption of xenon in a series of zinc metal–organic frameworks, IRMOFs, has been studied by xenon NMR spectroscopy [197,198]. Each framework has a cubic cage whose size depends on the organic linker molecule. Compared with X-ray crystallography, the NMR results show that the relationship between the cage size and the ^{129}Xe chemical shift is not totally obvious. The observed discrepancies may be due to the differences in the chemical composition and morphology of the surfaces of the IRMOFs compared to the silicate materials (MCM-41, zeolites) from which the chemical shift-pore size correlation is derived. To modify the pore environment,

functional groups were added to the phenylene rings. For example, IRMOF-2 has been brominated at position 2.

Figure 27 shows the variable-temperature HP ^{129}Xe spectra of IRMOF-2. At room temperature, two intense partially-resolved signals at 62 and 70 ppm along with the weak free gas peak at 0 ppm are observed. When the sample is cooled to -100 °C, the chemical shifts increase and become completely resolved, centered at 85 and 165 ppm. The abrupt chemical shift change of the downfield peak at the lowest temperatures may imply the presence of a new adsorption site. This new adsorption site is likely to have a slightly longer retention time for xenon at low temperature and therefore slower exchange between the adsorption sites. The slower exchange prevents the xenon atoms from sampling all available void space during the NMR acquisition time and results in separate peaks with shifts not averaged over all possible adsorption sites.

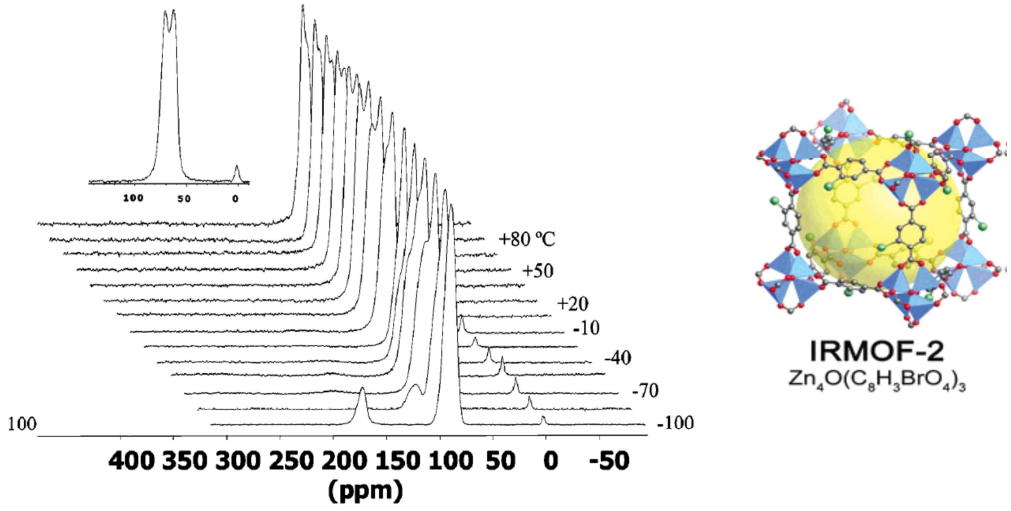

Figure 27. Variable-temperature HP ^{129}Xe NMR spectra for IRMOF-2. Adapted from reference [198] with permission.

Comotti *et al.* [199] demonstrate the open pore structure and the easy accessibility of the nanochannels of aluminum naphthalenedicarboxylate Al(OH)(1,4-NDC) $2H_2O$ compound. From theoretical and experimental studies of ^{129}Xe NMR on zeolites the authors deduce that a chemical shift value of 72 ppm, corresponds to a pore size of 9 Å which is consistent with square-shaped channels of 7.7×7.7 $Å^2$ cross section and a diagonal size of 10.5 Å. 2D EXSY, showed that the exchange time between gas and adsorbed phase is as short as 15 ms proving that the nanopores are open and easily accessible by the gas phase. Through variable-temperature HP ^{129}Xe NMR experiments the authors were able to achieve a fine description of the large nanochannel space and surface area. From the fitting of the chemical shift data as a function of temperature, the enthalpy of adsorption of 10 kJ/mol has been evaluated.

Cadmium and zinc hexacyanocobaltates(III) were studied by Lima *et al.* [200]. The crystal structures of these two compounds are representative of porous hexacyanometallates, cubic (*Fm*-3*m*) for cadmium and rhombohedral (*R*-3*c*) for zinc. In the cubic structure, the porosity is related to systematic vacancies created from the elemental building block leading to a network of large pores (ca. 8.5 Å) connected by relatively small windows (ca. 4.2 Å) (interstitial free spaces). The rhombohedral (*R*-3*c*) structure is free of vacant sites but has tetrahedral coordination for the zinc atom, which leads to relatively large ellipsoidal cavities (ca. 5.1×12.7×8.3 Å) communicating through elliptical windows (ca. 3.9×5.2 Å).

For the cadmium compound, up to 2 Xe atoms per cavity are adsorbed, which is ascribed to a relatively strong adsorption field for Xe within the pores. This is probably related to the existence of an electric field gradient at the pore surface. A significantly weaker guest-host interaction was observed for the rhombohedral zinc structure, in

which the pore surface has practically nonpolar character. The pore diameter estimated from the chemical shift is in close agreement with the pore volume estimated from the crystal structure and the degree of hydration. In the rhombohedral phase, the anisotropy of the signals shows a marked dependence on the number of Xe atoms within the porous framework, ascribed to Xe-Xe interactions.

It has been observed that the framework of hybrid materials may be highly flexible with a change of the cell volume by more than 300% sometimes [201]. The pore structure may expand or contract under stimuli like temperature or gas adsorption. The (Al or Cr) MIL-53 metal-organic framework material has attracted a lot of attention on account of its important flexibility and the occurrence of an oscillation (or “breathing”) during adsorption between two distinct conformations called the large-pore phase (lp) and the narrow-pore phase (np), which have a remarkable difference in cell volume of up to 40% [202–205].

The two conformations are easily distinguished by ^{129}Xe NMR and the transition between the two stable states has been thoroughly studied by Springuel-Huet *et al.* [206]. At room temperature, the dehydrated solid adopts the *lp* form. It corresponds to the narrow line observed at low Xe pressures (Figure 28). As Xe pressure increases, a broad anisotropic line appears at higher chemical shift due to the transformation of some *lp* channels into *np* ones. In the pressure range studied, the two lines co-exist revealing that the transformation is not complete at room temperature. Determining the local Xe loading in *lp* channels from the chemical shift variation versus Xe loading obtained at low Xe pressure before the *lp*/*np* transition, the measurement of the signal intensities makes it possible to estimate the rate of transformation as a function of Xe pressure. It rapidly reaches a limited value of about 72%.

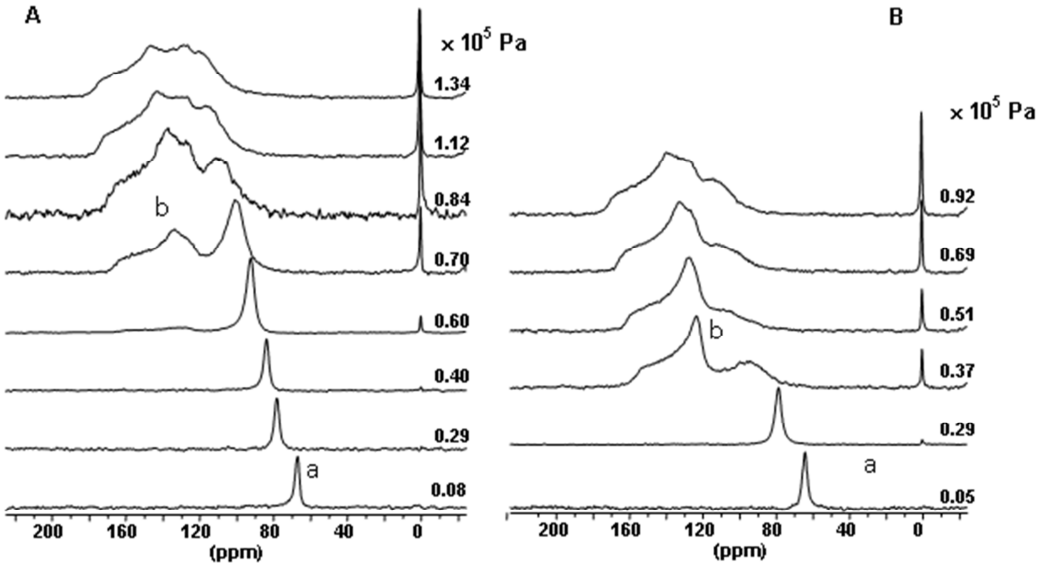

Figure 28. ^{129}Xe NMR spectra versus xenon pressure (thermally-polarized ^{129}Xe) recorded at adsorption (A) and desorption (B). From reference [206] with permission.

More interestingly, the chemical shift variation of the *lp* line versus Xe pressure exhibits a hysteresis (Figure 29). Actually, at desorption, the chemical shift first remains roughly constant. Then, it recovers its initial value as soon as the *np* line disappears. This proves that the Xe concentration remains constant in *lp* channels as long as *np* channels exist. This observation led us to propose the following mechanism of transformation: when the Xe loading reaches a critical value (2 Xe atoms per u. c.), the interaction between Xe and the pore surface is strong enough to induce the closing of the channels, the process starting from their extremities toward the center. In the present conditions (temperature and Xe pressure), the middle part of the channels remains in *lp* form so that the adsorbed Xe atoms are no longer in equilibrium with the outer gas phase. Low-temperature HP experiments show that the transformation can be complete even at low pressure (at 221 K and 1.33 kPa). At the opposite, at 343 K, the structure remains open (*lp* form) even at high Xe pressure.

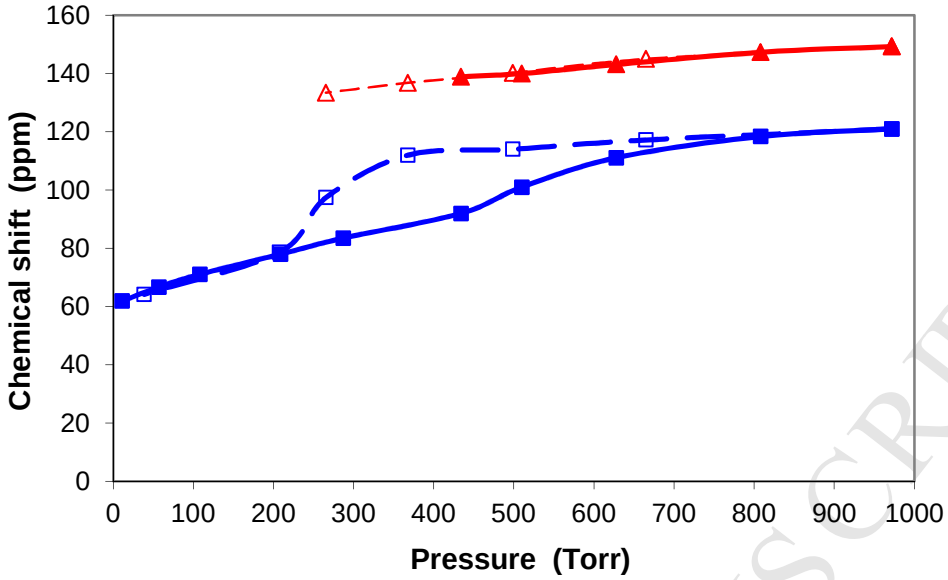

Figure 29. Chemical shift variations of *lp* (blue) and *np* (red) lines as a function of pressure. Adsorption: full symbols; desorption: empty symbols. Adapted from reference [206] with permission.

Besides the "breathing" effect fully demonstrated by the MIL-53 solids, the framework flexibility of MOFs can lead to another phenomenon, namely the "gate pressure" effect. Some hybrid materials present no permanent porosity but may adsorb molecules above a threshold pressure of the adsorptive. The so-called “gate-pressure” effect of a novel MOF denoted as DUT-8(Ni) has been studied by Klein *et al.* [207]. This MOF showed reversible structural transformation without loss of crystallinity upon solvent removal and gas adsorption.

In another paper, Hoffmann *et al.* have used high-pressure in situ ^{129}Xe NMR spectroscopy in order to study this novel MOF [208]. One major observation was the appearance, at high pressure (14 bar) of a narrow signal at ca. 220–230 ppm due to xenon adsorbed inside the pore system of DUT-8(Ni) in its open state (Figure 30). The high ^{129}Xe chemical shift is due to the great amount of adsorbed xenon as measured by

adsorption experiments. A paramagnetic shift of the order of 20 ppm, determined by magnetization measurements, may also contribute to the high chemical shift value observed for DUT-8(Ni) [207].

More recently xenon adsorption studies combined with ^{129}Xe NMR spectroscopy were used to study the flexibility of a series of DUT-8(M), (M = Ni, Co, Cu, Zn) compounds [209,210]. Depending on the metal atom, the compounds show reversible (DUT-8(Ni), DUT-8(Co)), non-reversible (DUT-8(Zn)) or no (DUT-8(Cu)) structural transformation upon solvent removal and/or physisorption of several gases.

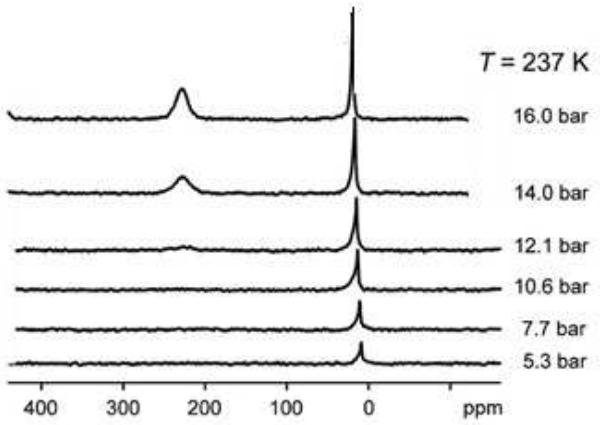

Figure 30. ^{129}Xe NMR spectra measured at 237 K and various pressures on DUT-8(Ni) with initially “closed” pore system. The pore system opens at a gate pressure of ca. 12 bar. Adapted from reference [208] with permission.

8.3. Periodic Mesoporous Organosilicas

Periodic mesoporous organosilica materials (PMO) are distinguished from other ordered mesoporous materials by the chemical composition of its pore wall, which is made of organosilica in which each individual organic group is covalently bonded to two or more silicon atoms. PMOs are widely used as functional materials, adsorbents and catalysts [211,212].

Periodic mesoporous hybrid p-phenylenesilica presenting crystalline order in the walls have been studied by Comotti *et al*. [213]. The open pore structure and the easy accessibility of the nanochannels to the gas phase have been demonstrated by (HP) xenon NMR, under extreme xenon dilution. A precise description of PMO nanochannels has been obtained using variable-temperature HP ^{129}Xe NMR experiments. A physisorption energy of 13.9 kJ mol^{-1} has been extracted from the above experiments.

9. Miscellaneous: carbon, soils and stones

a) Carbon

Porous carbon materials with high specific surface areas and superhydrophobicity have attracted much research interest due to their potential application in various fields including adsorption/separation of gases [214], energy storage [215] and catalysis [216]. Mesoporous carbon materials can be synthesized using methods based on soft-templating [217] or hard-templating (denoted also nano-casting) [218]. As has been shown by Romanenko *et al.*, the chemical shift is very sensitive to the presence of oxygen-containing functional groups on the surface of mesoporous carbon materials [219].

One of the most widely known class of materials produced by nano-casting are the so-called CMKs [220].

They are produced by infiltration of carbon sources (e.g., sucrose) into ordered mesoporous silica (followed by carbonization and template removal). The resulting carbon materials offer ordered systems with uniform pores.

In the literature, ^{129}Xe NMR spectra recorded on activated carbon [221], carbon filaments [222], as well as carbon nanotubes [223,224] present only one signal for adsorbed Xe.

In 2009, Onfroy *et al.* have shown that, in addition to the peak corresponding to the mesopores, another line is detected for CMK-3 due to xenon adsorbed in micropores [225]. In order to study the connectivity between these two types of pores, 2D EXSY experiments were carried out (Figure 31).

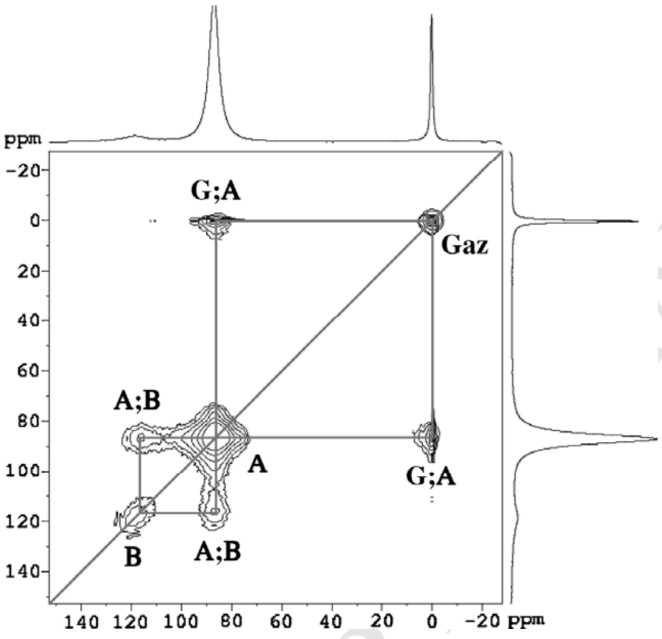

Figure 31. ^{129}Xe 2D-EXSY map of xenon adsorbed in CMK-3 at 295 K (P_{Xe} = 53 kPa, mixing time = 50 ms). From reference [225] with permission.

The 2D-exchange map reveals the presence of cross peaks between the gas phase (G) and the mesopores (A) and between the mesopores and micropores (B), which indicates the presence of microporosity inside the carbon rods. Similar results have been obtained by Oschatz *et al.* [226]. However, the xenon experiments performed at high pressure on hierarchical ordered mesoporous carbide-derived carbons (OM-CDC) exhibit one peak due to the well-connected pore systems allowing fast exchange of adsorbed xenon. The

CMK-3 hierarchical sample containing micropores and mesopores was characterized after n-nonane loading using ^{129}Xe NMR [226]. Actually, the adsorption of n-nonane is used to block the micropores making them inaccessible for xenon or other molecules. Figure 32 shows the disappearance of the signal at 230 ppm due to the presence of micropores in CMK-3. However, the increase of the chemical shift of xenon in the mesopores after n-nonane indicates that the hydrocarbon can penetrate into the mesopores which become smaller. The strong interaction between xenon and nonane molecules may also contribute to this chemical shift increase.

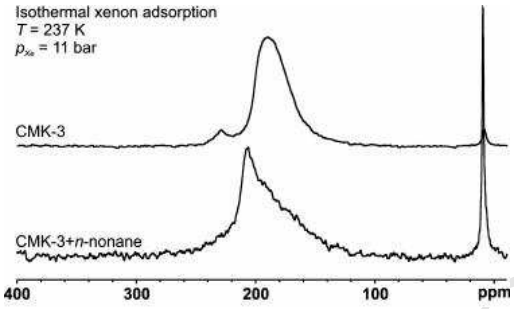

Figure 32. ^{129}Xe NMR spectra of the mesoporous sample CMK-3 OM-SiC-CDC-800 before and after loading with n-nonane measured at 237 K at a xenon pressure of 11 bars (p/p0=0.64). From reference [226] with permission.

b) Soils and stones

In the case of complex materials such as charcoals, ~~of~~ building stones composed of various minerals and ~~of~~ soils also composed of minerals as well as organic matter, ^{129}Xe NMR spectroscopy has been revealed to be useful for characterizing the porosity and the state of the surface [227–229]. In such complex media, the chemical shift cannot be interpreted quantitatively, and then the ^{129}Xe spectra are rather fingerprints of the materials.

An unusual fact has been observed with charcoals, the HP and TP spectra are different [228]. This may occur with heterogeneous materials because HP ^{129}Xe does not probe the whole sample as TP ^{129}Xe does. Actually, in HP experiments, the signal comes from Xe diffusing in easily accessible regions, often the peripheral of the particles/crystallites and its intensity depends not only on the longitudinal relaxation time but also on the exchange rate between depolarized ^{129}Xe (hyperpolarisation is destroyed by the radiofrequency pulse) and freshly hyperpolarized ^{129}Xe. In such situation, environments where ^{129}Xe depolarizes rapidly or/and Xe does not diffuse rapidly do not give rise to a detectable NMR signal as seen in Figure 33.

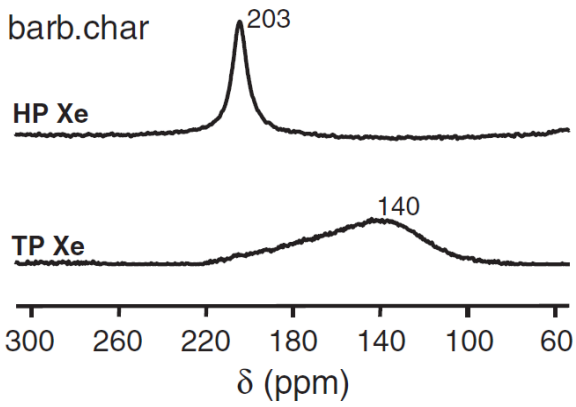

Figure 33. ^{129}Xe NMR spectra for the barbeque charcoals recorded respectively at P_{Xe}=400 (TP Xe) and 7 mbar (HP Xe). The chemical shift is pressure independent. Adapted from reference [228] with permission.

Nevertheless, one must keep in mind that the HP signal may highlight an environment which may correspond to a small fraction of the whole materials sample and therefore correspond to weak intensity (even non detected) in the TP spectrum.

Studying different Italian rocks used as buildings stones in applications like urban furniture, funeral art, Mauri and Simonutti obtained complex spectra presenting several overlapping signals [229]. Among them some have negative chemical shift. The

observation of negative chemical shifts is rare. As far as we know, the only example is the case of Ag-exchanged zeolite for which chemical shifts as low as -50 ppm have been observed [230]. They were attributed to specific interaction (leading to Xe nuclei shielding) between Xe atoms and Ag^+ cations having a nd^{10} electronic configuration. In the present study, they were attributed to the presence of phyllosilicate minerals with high surface areas such as chrysotile formed by bundles of fibrils (diameter < 1 μm), composed themselves of microfibrils (diameter < 50 nm). Chrysotile is a natural magnesium silicate containing many metals at ppm level. Among them, Cu^+ has also a nd^{10} electronic configuration. The authors suggest that Cu^+ cations are concentrated at the fibrils' surface and provide a measurable effect.

10. Supramolecular compounds

During the last decade, supramolecular complexes have been widely used as biosensors for MRI applications. Xenon encapsulated into cryptophane derivative cages can be detected and exploited by NMR spectroscopy. The great sensitivity of xenon to local environment combined with the use of hyperpolarization techniques led to an important variation of the NMR chemical shifts [231–233]. Additional signal amplification can be obtained by chemical exchange saturation transfer (hyperCEST) [234,235].

According to this biosensing concept, encapsulated xenon has a resonance frequency that is completely different from the frequency of free xenon. Moreover the chemical shift of caged xenon varies when the host system is in the presence of the targeted receptor or analyte. Cryptophane encapsulated Xe can also be used as temperature sensor due to the linear temperature dependence of its chemical shift and even as local pH sensors [236,237].

Very recently, Roukala *et al.* showed that metallosupramolecular cages Fe_4L_6 has a great affinity for xenon in solution. This study demonstrates the potential of metallosupramolecular cages to extract rare gases [238].

11. Conclusion

The main objective of this review was to reveal a part of the great potential of ^{129}Xe NMR using the extreme sensitivity of the xenon atom to its physical and chemical environment. In this paper, the principles and applications of the Xe-NMR technique for characterizing porous materials were reviewed. This review covers the most current and advanced Xenon NMR research studies since 2005.

In the first part of this review, the basic principle of ^{129}Xe NMR spectroscopy of xenon adsorbed on porous materials is introduced. The fast exchange model which allows the quantitative evaluation of the pore size is developed. The two most common approaches to hyperpolarized ^{129}Xe via Spin-Exchange Optical Pumping (SEOP) were also summarized.

The second part of this work reports applications of TP and HP ^{129}Xe NMR spectroscopy to probe various types of porous materials. Characterization of microporous solids and especially zeolite type materials with a special focus on issues as the evaluation of pore size and connectivity, the location of extraframework species as well as monitoring zeolite nucleation / collapse were reported. The use of xenon NMR on mesoporous, hierarchical, organic and hybrid porous materials was reported and commented. Based on these applications, the high potential of ^{129}Xe NMR technique to explore the surface porosity of porous solids was exposed.

Different reviews on xenon have already been published. This one focused mainly on the understanding of the properties of new and advanced materials, as powder, films or extrudates. However, this review clearly shows that few studies on the dynamics of xenon in porous materials were carried out. Further works on the dynamic NMR parameters in porous media will contribute to a better understanding of the different interactions experienced by xenon atoms. Moreover, theoretical studies on the nature of these Xe-host interactions are needed. They would lead to the driving forces of these interactions.

Though the use of hyper- polarized (HP) xenon has allowed great extension of the possible applications in particular to solids available in small quantity (films), with low surface area or having long relaxation time (T_1), this technique is not suitable for materials containing paramagnetic impurities leading to short T_1 as shown recently for hydrotreatment alumina catalysts.

Despite the tremendous progress in the HP Xenon NMR to probe the porosity of a wide range of materials, a keen interest is noticeable in biosensing and in MR imaging for the early detection of biological events (cancers).

Finally, Xenon NMR sprectroscopy is not intended to replace other characterization techniques, but it can be a convenient complementary technique for exploring textural and transport properties of porous media.

Acknowledgments

IFP Energies nouvelles is gratefully acknowledged for financial support through the PhD grant of E. Weiland.

References

[1] S. Seidel, K. Seppelt, Science 290 (2000) 117–118.
[2] I. Dmochowski, Nat. Chem. 1 (2009) 250–250.
[3] W.G. Proctor, F.C. Yu, Phys. Rev. 81 (1951) 20.
[4] T. Ito, J. Fraissard, Proc Int Conf Zeolites 5th (1980) 510–15.
[5] J.A. Ripmeester, D.W. Davidson, J. Mol. Struct. 75 (1981) 67–72.
[6] T. Ito, L.C. De Menorval, J.P. Fraissard, J. Chim. Phys. Phys.-Chim. Biol. 80 (1983) 573–8.
[7] B.F. Chmelka, R. Ryoo, S.B. Liu, L.C. De Menorval, C.J. Radke, E.E. Petersen, A. Pines, J. Am. Chem. Soc. 110 (1988) 4465–7.
[8] D.H. Ahn, J.S. Lee, M. Nomura, W.M.H. Sachtler, G. Moretti, S.I. Woo, R. Ryoo, J. Catal. 133 (1992) 191–201.
[9] S.J. Cho, S.M. Jung, Y.G. Shul, R. Ryoo, J. Phys. Chem. 96 (1992) 9922–7.
[10] S.J. Cho, W.-S. Ahn, S.B. Hong, R. Ryoo, J. Phys. Chem. 100 (1996) 4996–5003.
[11] D. Rouabah, J. Fraissard, Solid State Nucl. Magn. Reson. 3 (1994) 153–62.
[12] M.D. Sefcik, J. Schaefer, J.A.E. Desa, W.B. Yelon, Polym. Prepr. Am. Chem. Soc. Div. Polym. Chem. 24 (1983) 85–6.
[13] T.R. Stengle, K.L. Williamson, Macromolecules 20 (1987) 1428–30.
[14] G.J. Kennedy, Polym. Bull. Berl. Ger. 23 (1990) 605–8.
[15] A.P.M. Kentgens, H.A. Van Boxtel, R.J. Verweel, W.S. Veeman, Macromolecules 24 (1991) 3712–14.
[16] J.H. Walton, Polym. Polym. Compos. 2 (1994) 35–41.
[17] F.M. Mirabella, D.C. McFaddin, Polymer 37 (1996) 931–8.
[18] F. Junker, W.S. Veeman, Macromolecules 31 (1998) 7010–7013.
[19] T.J. Lowery, S.M. Rubin, E.J. Ruiz, M.M. Spence, N. Winssinger, P.G. Schultz, A. Pines, D.E. Wemmer, Magn. Reson. Imaging 21 (2003) 1235–1239.
[20] T.J. Lowery, S.M. Rubin, E.J. Ruitz, A. Pines, D.E. Wemmer, Angew. Chem. Int. Ed. 43 (2004) 6320–6322.
[21] M.M. Spence, E.J. Ruiz, S.M. Rubin, T.J. Lowery, N. Winssinger, P.G. Schultz, D.E. Wemmer, A. Pines, J. Am. Chem. Soc. 126 (2004) 15287–15294.
[22] S.-I. Han, S. Garcia, T.J. Lowery, E.J. Ruiz, J.A. Seeley, L. Chavez, D.S. King, D.E. Wemmer, A. Pines, Anal. Chem. 77 (2005) 4008–4012.
[23] T.J. Lowery, M. Doucleff, E.J. Ruiz, S.M. Rubin, A. Pines, D.E. Wemmer, Protein Sci. 14 (2005) 848–855.
[24] J. Jokisaari, P. Diehl, O. Muenster, Mol. Cryst. Liq. Cryst. 188 (1990) 189–96.
[25] O. Muenster, J. Jokisaari, P. Diehl, Mol. Cryst. Liq. Cryst. 206 (1991) 179–86.
[26] J. Lounila, O. Muenster, J. Jokisaari, P. Diehl, J. Chem. Phys. 97 (1992) 8977–85.
[27] J. Bharatam, C.R. Bowers, J. Phys. Chem. B 103 (1999) 2510–2515.
[28] M. Ylihautala, J. Lounila, J. Jokisaari, J. Chem. Phys. 110 (1999) 6381–6388.
[29] C.J. Jameson, A.C. de Dios, J. Chem. Phys. 97 (1992) 417–434.
[30] C.J. Jameson, A.K. Jameson, H.M. Lim, B.I. Baello, J. Chem. Phys. 100 (1994) 5977–87.
[31] C.J. Jameson, A.K. Jameson, B.I. Baello, H.-M. Lim, J. Chem. Phys. 100 (1994) 5965–5976.
[32] C.J. Jameson, H.-M. Lim, J. Chem. Phys. 103 (1995) 3885–94.
[33] A.C. de Dios, C.J. Jameson, J. Chem. Phys. 107 (1997) 4253–4270.

[34] C.J. Jameson, J. Chem. Phys. 116 (2002) 8912–8929.
[35] D. Canet, Nuclear Magnetic Resonance: Concepts and Methods, John Wiley & Sons, Inc., New York, 1996.
[36] M.H. Levitt, Spin Dynamics: Basics of Nuclear Magnetic Resonance, 2nd Edition, Wiley-Blackwell, 2008.
[37] A. Nossov, F. Guenneau, M.-A. Springuel-Huet, E. Haddad, V. Montouillout, B. Knott, F. Engelke, C. Fernandez, A. Gédéon, Phys. Chem. Chem. Phys. 5 (2003) 4479–4483.
[38] S. Pawsey, K.K. Kalebaila, I. Moudrakovski, J.A. Ripmeester, S.L. Brock, J. Phys. Chem. C 114 (2010) 13187–13195.
[39] K. Knagge, J.R. Smith, L.J. Smith, J. Buriak, D. Raftery, Solid State Nucl. Magn. Reson. 29 (2006) 85–89.
[40] C. Dybowski, N. Bansal, T.M. Duncan, Annu. Rev. Phys. Chem. 42 (1991) 433–64.
[41] P.J. Barrie, J. Klinowski, Prog. Nucl. Magn. Reson. Spectrosc. 24 (1992) 91–108.
[42] D. Raftery, B. Chmelka, in:, B. Blümich (Ed.), Solid-State NMR Methods, Springer Berlin Heidelberg, 1994, pp. 111–158.
[43] C.I. Ratcliffe, Annu. Rep. NMR Spectrosc. 36 (1998) 123–221.
[44] J.-L. Bonardet, J. Fraissard, A. Gédéon, M.-A. Springuel-Huet, Catal. Rev. - Sci. Eng. 41 (1999) 115–225.
[45] T. Pietrass, Magn. Reson. Rev. 17 (2000) 263–337.
[46] D. Raftery, Annu. Rep. NMR Spectrosc. 57 (2006) 205–270.
[47] R. Grosse, R. Burmeister, B. Boddenberg, A. Gedeon, J. Fraissard, J. Phys. Chem. 95 (1991) 2443–7.
[48] J.L. Bonardet, A. Gedeon, J. Fraissard, Stud. Surf. Sci. Catal. 94 (1995) 139–46.
[49] M.A.M. Forgeron, R.E. Wasylishen, M. Gerken, G.J. Schrobilgen, Inorg. Chem. 46 (2007) 3585–3592.
[50] M. Gerken, G.L. Schrobilgen, Coord. Chem. Rev. 197 (2000) 335–395.
[51] M.A. Springuel-Huet, J.L. Bonardet, J. Fraissard, Appl. Magn. Reson. 8 (1995) 427–56.
[52] A. Gedeon, J. Fraissard, Chem. Phys. Lett. 219 (1994) 440–4.
[53] T. Ito, J. Fraissard, J. Chem. Phys. 76 (1982) 5225–9.
[54] C.J. Jameson, A.K. Jameson, S.M. Cohen, J. Chem. Phys. 59 (1973) 4540–6.
[55] V.V. Terskikh, I.L. Mudrakovskii, V.M. Mastikhin, J. Chem. Soc. Faraday Trans. 89 (1993) 4239–43.
[56] I.L. Moudrakovski, C.I. Ratcliffe, J.A. Ripmeester, Appl. Magn. Reson. 8 (1995) 385–399.
[57] C.J. Jameson, A.K. Jameson, R.E. Gerald, H.-M. Lim, J. Phys. Chem. B 101 (1997) 8418–8437.
[58] L.C. De Menorval, J.P. Fraissard, T. Ito, J. Chem. Soc. Faraday Trans. 1 Phys. Chem. Condens. Phases 78 (1982) 403–10.
[59] T. Ito, J. Fraissard, J. Chem. Soc. Faraday Trans. 1 Phys. Chem. Condens. Phases 83 (1987) 451–62.
[60] M.A. Springuel-Huet, J. Fraissard, Chem. Phys. Lett. 154 (1989) 299–302.
[61] T. Koskela, J. Jokisaari, C. Satyanarayana, Microporous Mesoporous Mater. 67 (2004) 113–122.
[62] V.V. Terskikh, I.L. Moudrakovski, H. Du, C.I. Ratcliffe, J.A. Ripmeester, J. Am. Chem. Soc. 123 (2001) 10399–10400.

[63] D. Raftery, H. Long, T. Meersmann, P.J. Grandinetti, L. Reven, A. Pines, Phys. Rev. Lett. 66 (1991) 584–7.
[64] T.G. Walker, W. Happer, Rev. Mod. Phys. 69 (1997) 629.
[65] T.G. Walker, in:, J Phys Conf Ser, 2011, p. 012001.
[66] B. Driehuys, G.D. Cates, E. Miron, K. Sauer, D.K. Walter, W. Happer, Appl. Phys. Lett. 69 (1996) 1668–1670.
[67] M. Haake, A. Pines, J.A. Reimer, R. Seydoux, J. Am. Chem. Soc. 119 (1997) 11711–11712.
[68] E. Brunner, R. Seydoux, M. Haake, A. Pines, J.A. Reimer, J. Magn. Reson. 130 (1998) 145–148.
[69] M. Hunger, T. Horvath, J. Chem. Soc. Chem. Commun. (1995) 1423–1424.
[70] I.C. Ruset, S. Ketel, F.W. Hersman, Phys. Rev. Lett. 96 (2006) 053002.
[71] H. Imai, J. Fukutomi, A. Kimura, H. Fujiwara, Concepts Magn. Reson. Part B Magn. Reson. Eng. 33B (2008) 192–200.
[72] P. Nikolaou, A.M. Coffey, L.L. Walkup, B.M. Gust, N. Whiting, H. Newton, S. Barcus, I. Muradyan, M. Dabaghyan, G.D. Moroz, M.S. Rosen, S. Patz, M.J. Barlow, E.Y. Chekmenev, B.M. Goodson, Proc. Natl. Acad. Sci. 110 (2013) 14150–14155.
[73] A.L. Zook, B.B. Adhyaru, C.R. Bowers, J. Magn. Reson. 159 (2002) 175–182.
[74] P. Nikolaou, A.M. Coffey, L.L. Walkup, B.M. Gust, N. Whiting, H. Newton, I. Muradyan, M. Dabaghyan, K. Ranta, G.D. Moroz, M.S. Rosen, S. Patz, M.J. Barlow, E.Y. Chekmenev, B.M. Goodson, Magn. Reson. Imaging 32 (2014) 541–550.
[75] P. Nikolaou, A.M. Coffey, L.L. Walkup, B.M. Gust, C.D. LaPierre, E. Koehnemann, M.J. Barlow, M.S. Rosen, B.M. Goodson, E.Y. Chekmenev, J. Am. Chem. Soc. 136 (2014) 1636–1642.
[76] P. Nikolaou, A.M. Coffey, K. Ranta, L.L. Walkup, B.M. Gust, M.J. Barlow, M.S. Rosen, B.M. Goodson, E.Y. Chekmenev, J. Phys. Chem. B 118 (2014) 4809–4816.
[77] N. Whiting, P. Nikolaou, N.A. Eschmann, B.M. Goodson, M.J. Barlow, J. Magn. Reson. 208 (2011) 298–304.
[78] N. Whiting, P. Nikolaou, N.A. Eschmann, M.J. Barlow, R. Lammert, J. Ungar, W. Hu, L. Vaissie, B.M. Goodson, Appl. Phys. B 106 (2012) 775–788.
[79] P. Nikolaou, A.M. Coffey, M.J. Barlow, M.S. Rosen, B.M. Goodson, E.Y. Chekmenev, Anal. Chem. 86 (2014) 8206–8212.
[80] S.E. Korchak, W. Kilian, L. Mitschang, Appl. Magn. Reson. 44 (2013) 65–80.
[81] T. Maly, G.T. Debelouchina, V.S. Bajaj, K.-N. Hu, C.-G. Joo, M.L. Mak–Jurkauskas, J.R. Sirigiri, P.C.A. van der Wel, J. Herzfeld, R.J. Temkin, R.G. Griffin, J. Chem. Phys. 128 (2008) 052211.
[82] A. Capozzi, C. Roussel, A. Comment, J.-N. Hyacinthe, J. Phys. Chem. C 119 (2015) 5020–5025.
[83] E.V. Krjukov, J.D. O'Neill, J.R. Owers-Bradley, J. Low Temp. Phys. 140 (2005) 397–408.
[84] A. Honig, X. Wei, A. Lewis, E. ter Haar, K. Seraji-Bozorgzad, Phys. B Condens. Matter Amst. 284-288 (2000) 2049–2050.
[85] J.W. McNabb, D.N. Balakishiyeva, A. Honig, J. Magn. Reson. 188 (2007) 206–215.
[86] N. Biskup, N. Kalechofsky, D. Candela, Phys. B Condens. Matter Amst. Neth. 329-333 (2003) 437–438.

[87] J.D. O'Neill, E.V. Krjukov, J.R. Owers-Bradley, Y. Xia, J. Low Temp. Phys. 146 (2007) 563–579.
[88] J. Demarquay, J. Fraissard, Chem. Phys. Lett. 136 (1987) 314–18.
[89] V.V. Terskikh, I.L. Moudrakovski, S.R. Breeze, S. Lang, C.I. Ratcliffe, J.A. Ripmeester, A. Sayari, Langmuir 18 (2002) 5653–5656.
[90] L. Itani, Y. Liu, W. Zhang, K.N. Bozhilov, L. Delmotte, V. Valtchev, J. Am. Chem. Soc. 131 (2009) 10127–10139.
[91] M.G. Samant, L.C. De Menorval, R.A. Dalla Betta, M. Boudart, J. Phys. Chem. 92 (1988) 3937–8.
[92] B.F. Chmelka, D. Raftery, A.V. McCormick, L.C. De Menorval, R.D. Levine, A. Pines, Phys. Rev. Lett. 66 (1991) 580–3.
[93] B.F. Chmelka, D. Raftery, A.V. McCormick, L.C. De Menorval, R.D. Levine, A. Pines, Phys. Rev. Lett. 67 (1991) 931.
[94] A.K. Jameson, C.J. Jameson, A.C. de Dios, E. Oldfield, R.E. Gerald, G.L. Turner, Solid State Nucl. Magn. Reson. 4 (1994) 1–12.
[95] C.J. Jameson, A.K. Jameson, H.-M. Lim, J. Chem. Phys. 104 (1996) 1709–28.
[96] C.J. Jameson, A.K. Jameson, H.-M. Lim, J. Chem. Phys. 107 (1997) 4364–4372.
[97] C.J. Jameson, A.K. Jameson, P. Kostikin, B.I. Baello, J. Chem. Phys. 112 (2000) 323–334.
[98] T.T.P. Cheung, J. Phys. Chem. 94 (1990) 376–80.
[99] D.N. Sears, B.A. Demko, K.J. Ooms, R.E. Wasylishen, Y. Huang, Chem. Mater. 17 (2005) 5481–5488.
[100] E. Lima, P. Bosch, S. Bulbulian, Appl. Radiat. Isot. 65 (2007) 259–265.
[101] L. Wang, P. Tian, Y. Yuan, M. Yang, D. Fan, H. Zhou, W. Zhu, S. Xu, Z. Liu, Microporous Mesoporous Mater. 196 (2014) 89–96.
[102] A. Corma, Nature 396 (1998) 353.
[103] M. Climent, A. Corma, V. Fornés, H. Garcia, S. Iborra, J. Miralles, Stud. Surf. Sci. Catal. 135 (2001) 235.
[104] M.-A. Springuel-Huet, F. Guenneau, A. Gédéon, A. Corma, J. Phys. Chem. C 111 (2007) 5694–5700.
[105] A. Gedeon, T. Ito, J. Fraissard, Zeolites 8 (1988) 376–80.
[106] R. Ryoo, S.B. Liu, L.C. De Menorval, K. Takegoshi, B. Chmelka, M. Trecoske, A. Pines, J. Phys. Chem. 91 (1987) 6575–7.
[107] L.C. De Menorval, D. Raftery, S.B. Liu, K. Takegoshi, R. Ryoo, A. Pines, J. Phys. Chem. 94 (1990) 27–31.
[108] B.F. Chmelka, J.G. Pearson, S.B. Liu, R. Ryoo, L.C. De Menorval, A. Pines, J. Phys. Chem. 95 (1991) 303–10.
[109] J.F. Wu, T.L. Chen, L.J. Ma, M.W. Lin, S.B. Liu, Zeolites 12 (1992) 86–94.
[110] S.B. Liu, L.J. Ma, M.W. Lin, J.F. Wu, T.L. Chen, J. Phys. Chem. 96 (1992) 8120–5.
[111] T. Ito, J.L. Bonardet, J. Fraissard, J.B. Nagy, C. Andre, Z. Gabelica, E.G. Derouane, Appl. Catal. 43 (1988) L5–L11.
[112] M.C. Barrage, J.L. Bonardet, J. Fraissard, Catal. Lett. 5 (1990) 143–154.
[113] J.T. Miller, B.L. Meyers, G.J. Ray, J. Catal. 128 (1991) 436–46.
[114] S.B. Liu, S. Prasad, J.F. Wu, L.J. Ma, T.C. Yang, J.T. Chiou, J.Y. Chang, T.C. Tsai, J. Catal. 142 (1993) 664–71.
[115] C. Tsiao, C. Dybowski, A.M. Gaffney, J.A. Sofranko, J. Catal. 128 (1991) 520–5.
[116] M.C. Barrage, J.L. Bonardet, J. Fraissard, Catal. Lett. 5 (1990) 143–54.

[117] G. Kostrab, D. Mravec, M. Bajus, I. Janotka, Y. Sugi, S.J. Cho, J.H. Kim, Appl. Catal. A 299 (2006) 122–130.
[118] X. Li, W. Zhang, S. Liu, L. Xu, X. Han, X. Bao, J. Catal. 250 (2007) 55–66.
[119] A. Guzmán-Vargas, E. Lima, G. Delahay, B. Coq, V. Lara, Ind. Eng. Chem. Res. 45 (2006) 4163–4168.
[120] E. Lima, A. Guzmán-Vargas, J. Méndez-Vivar, H. Pfeiffer, J. Fraissard, Catal. Lett. 120 (2008) 244–251.
[121] C. Daniel, A. Elbaraoui, S. Aguado, M.-A. Springuel-Huet, A. Nossov, J.-P. Fontaine, S. Topin, T. Taffary, L. Deliere, Y. Schuurman, D. Farrusseng, J. Phys. Chem. C 117 (2013) 15122–15129.
[122] P. Sozzani, S. Bracco, A. Comotti, M. Mauri, R. Simonutti, P. Valsesia, Chem. Commun. (2006) 1921–1923.
[123] A.O. Shepard, Am Antiq 27 (1962) 565–566.
[124] H. Van Olphen, Science 154 (1966) 645–646.
[125] M. Sánchez del Río, A. Doménech, M.T. Doménech-Carbó, M.L. Vázquez de Agredos Pascual, M. Suárez, E. García-Romero, in:, Emilio Galàn and Arieh Singer (Ed.), Dev. Clay Sci., Elsevier, 2011, pp. 453–481.
[126] E. Lima, A. Guzmán, M. Vera, J.L. Rivera, J. Fraissard, J Phys Chem C 116 (2012) 4556–4563.
[127] J.A. Ripmeester, C.I. Ratcliffe, J. Phys. Chem. 94 (1990) 8773–6.
[128] D.H. Brouwer, S. Alavi, J.A. Ripmeester, Phys. Chem. Chem. Phys. 9 (2007) 1093–1098.
[129] K. Shin, I.L. Moudrakovski, M.D. Davari, S. Alavi, C.I. Ratcliffe, J.A. Ripmeester, CrystEngComm 16 (2014) 7209–7217.
[130] M. Zaheer, C.D. Keenan, J. Hermannsdörfer, E. Roessler, G. Motz, J. Senker, R. Kempe, Chem. Mater. 24 (2012) 3952–3963.
[131] C.T. Kresge, M.E. Leonowicz, W.J. Roth, J.C. Vartuli, J.S. Beck, Nature 359 (1992) 710–712.
[132] D. Zhao, Q. Huo, J. Feng, B.F. Chmelka, G.D. Stucky, J Am Chem Soc 120 (1998) 6024–6036.
[133] Y. Lu, R. Ganguli, C.A. Drewien, M.T. Anderson, C.J. Brinker, W.-X. Gong, Y. Guo, H. Soyez, B. Dunn, M.H. Huang, J.I. Zink, Nature 381 (1996) 589.
[134] D. Grosso, G.J. de A.A. Soler-Illia, F. Babonneau, C. Sanchez, A. Albouy, A. Brunet-Bruneau, A.R. Balkenende, Adv. Mater. 13 (2001) 1085.
[135] N. Mnasri, C. Charnay, L.-C. de Ménorval, Y. Moussaoui, E. Elaloui, J. Zajac, Microporous Mesoporous Mater. 196 (2014) 305–313.
[136] M.H. Nader, F. Guenneau, P. Salamé, F. Launay, V. Semmer, A. Gédéon, J. Phys. Chem. C 111 (2007) 13564–13569.
[137] W. Zhang, C.I. Ratcliffe, I.L. Moudrakovski, C.-Y. Mou, J.A. Ripmeester, Anal. Chem. 77 (2005) 3379–3382.
[138] A. Galarneau, M. Nader, F. Guenneau, F. Di Renzo, A. Gédéon, J. Phys. Chem. C 111 (2007) 8268–8277.
[139] E. Weiland, M.-A. Springuel-Huet, A. Nossov, F. Guenneau, A.-A. Quoineaud, A. Gédéon, J. Phys. Chem. C 119 (2015) 15285–15291.
[140] P. Euzen, P. Raybaud, X. Krokidis, H. Toulhoat, J.-L. Le Loarer, J.-P. Jolivet, C. Froidefond, in:, F. Schüth, K.S.W. Sing, J. Weitkamp (Eds.), Handb. Porous Solids, Wiley-VCH Verlag GmbH, 2002, pp. 1591–1677.
[141] R. Prins, V.H.J. De Beer, Somorjai, Catal. Rev. - Sci. Eng. 31 (n.d.) 1–41.

[142] K. Hagiwara, T. Ebihara, N. Urasato, T. Fujikawa, Appl. Catal. A 285 (2005) 132–138.
[143] K. Hagiwara, T. Ebihara, N. Urasato, T. Fujikawa, Appl. Catal. A 293 (2005) 56–63.
[144] K. Hagiwara, J. Jpn. Pet. Inst. 51 (2008) 32–41.
[145] V.-V. Telkki, J. Lounila, J. Jokisaari, J. Phys. Chem. B 109 (2005) 757–763.
[146] V.-V. Telkki, J. Lounila, J. Jokisaari, J. Phys. Chem. B 109 (2005) 24343–24351.
[147] V.-V. Telkki, J. Lounila, J. Jokisaari, J. Chem. Phys. 124 (2006) 034711.
[148] V.-V. Telkki, J. Lounila, J. Jokisaari, Magn. Reson. Imaging 25 (2007) 457–460.
[149] V.-V. Telkki, J. Lounila, J. Jokisaari, Phys. Chem. Chem. Phys. 8 (2006) 2072–2076.
[150] V.-V. Telkki, Xenon Porometry : A Novel Method for Characterization of Porous Materials by Means of ^{129}Xe NMR Spectroscopy of Xenon Dissolved in a Medium, PhD thesis, University of Oulu, Finland, 2006.
[151] S. Habib, F. Launay, M.-A. Springuel-Huet, F. Guenneau, V. Semmer-Herlédan, N.N. Tušar, V. Kaučič, A. Gédéon, New J. Chem. 30 (2006) 1163–1170.
[152] S. Habib, F. Launay, H.E. Zakhem, M. Mazaj, F. Guenneau, P. Beaunier, D. Brouri, N.N. Tušar, V. Kaučič, A. Gédéon, Mater. Res. Bull. 48 (2013) 1288–1295.
[153] S. Habib, F. Launay, M.-A. Springuel-Huet, F. Guenneau, M. Mazaj, N.N. Tušar, A. Gédéon, J. Porous Mater. 16 (2009) 349–359.
[154] Y. Liu, W. Zhang, Z. Liu, S. Xu, Y. Wang, Z. Xie, X. Han, X. Bao, J. Phys. Chem. C 112 (2008) 15375–15381.
[155] L.-H. Chen, S.-T. Xu, X.-Y. Li, G. Tian, Y. Li, J.C. Rooke, G.-S. Zhu, S.-L. Qiu, Y.-X. Wei, X.-Y. Yang, Z.-M. Liu, B.-L. Su, J. Colloid Interface Sci. 377 (2012) 368–374.
[156] K. Cho, H.S. Cho, L.-C. de Ménorval, R. Ryoo, Chem. Mater. 21 (2009) 5664–5673.
[157] A. van Miltenburg, L.C. de Ménorval, M. Stöcker, Catal. Today 168 (2011) 57–62.
[158] F. Chen, F. Deng, M. Cheng, Y. Yue, C. Ye, X. Bao, J. Phys. Chem. B 105 (2001) 9426–9432.
[159] T. Ito, M.A. Springuel-Huet, J. Fraissard, Zeolites 9 (1989) 68–73.
[160] Y. Liu, W. Zhang, S. Xie, L. Xu, X. Han, X. Bao, J. Phys. Chem. B 112 (2008) 1226–1231.
[161] S. Xie, S. Liu, Y. Liu, X. Li, W. Zhang, L. Xu, Microporous Mesoporous Mater. 121 (2009) 166–172.
[162] A. Comotti, R. Simonutti, S. Stramare, P. Sozzani, Nanotechnology 10 (1999) 70.
[163] I. Bassanetti, A. Comotti, P. Sozzani, S. Bracco, G. Calestani, F. Mezzadri, L. Marchiò, J. Am. Chem. Soc. 136 (2014) 14883–14895.
[164] P. Sozzani, A. Comotti, R. Simonutti, T. Meersmann, J.W. Logan, A. Pines, Angew. Chem. Int. Ed. 39 (2000) 2695–2698.
[165] R. Anedda, D.V. Soldatov, I.L. Moudrakovski, M. Casu, J.A. Ripmeester, Chem. Mater. 20 (2008) 2908–2920.
[166] C.-Y. Cheng, C.R. Bowers, J. Am. Chem. Soc. 129 (2007) 13997–14002.
[167] M. Dvoyashkin, A. Wang, S. Vasenkov, C.R. Bowers, J. Phys. Chem. Lett. 4 (2013) 3263–3267.

[168] D.H. Brouwer, I.L. Moudrakovski, K.A. Udachin, G.D. Enright, J.A. Ripmeester, Cryst. Growth Des. 8 (2008) 1878–1885.
[169] J.A. Ripmeester, C.I. Ratcliffe, J.S. Tse, J. Chem. Soc. Faraday Trans. 1 Phys. Chem. Condens. Phases 84 (1988) 3731–45.
[170] M. Springuel-Huet, J. Demarquay, T. Ito, J. Fraissard, Stud. Surf. Sci. Catal. 37 (1988) 183–9.
[171] I. Moudrakovski, D.V. Soldatov, J.A. Ripmeester, D.N. Sears, C.J. Jameson, Proc. Natl. Acad. Sci. U. S. A. 101 (2004) 17924–17929.
[172] A. Comotti, S. Bracco, L. Ferretti, M. Mauri, R. Simonutti, P. Sozzani, Chem. Commun. (2007) 350–352.
[173] M. Kotecha, W. Veeman, B. Rohe, M. Tausch, Microporous Mesoporous Mater. 95 (2006) 66–75.
[174] J. Weber, J. Schmidt, A. Thomas, W. Böhlmann, Langmuir 26 (2010) 15650–15656.
[175] R. Motoshige, Y. Mawatari, A. Motoshige, Y. Yoshida, T. Sasaki, H. Yoshimizu, T. Suzuki, Y. Tsujita, M. Tabata, J. Polym. Sci. Part Polym. Chem. (2013) n/a–n/a.
[176] D.E. Demco, C. Melian, J. Simmelink, V.M. Litvinov, M. Möller, Macromol. Chem. Phys. 211 (2010) 2611–2623.
[177] R. Simonutti, S. Bracco, A. Comotti, M. Mauri, P. Sozzani, Chem. Mater. 18 (2006) 4651–4657.
[178] M. Duewel, N. Vogel, C.K. Weiss, K. Landfester, H.-W. Spiess, K. Münnemann, Macromolecules 45 (2012) 1839–1846.
[179] S. Kariyo, M. Kuppers, V. Badiger Manohan, A. Prabhakar, B. Jagadeesh, S. Stapf, B. Blumich, Magn. Reson. Imaging 23 (2005) 249–53.
[180] S. Glöggler, M. Raue, J. Colell, P. Türschmann, A. Liebisch, T. Mang, B. Blümich, S. Appelt, ChemPhysChem 13 (2012) 4120–4123.
[181] H. Yoshimizu, in:, H.N. Cheng, T. Asakura, A.D. English (Eds.), NMR Spectrosc. Polym. Innov. Strateg. Complex Macromol., American Chemical Society, Washington, DC, 2011, pp. 509–523.
[182] H. Yoshimizu, S. Ohta, T. Asano, T. Suzuki, Y. Tsujita, Polym. J. 44 (2012) 821–826.
[183] E. Locci, P. Roose, K. Bartik, M. Luhmer, J. Colloid Interface Sci. 330 (2009) 344–351.
[184] T. Suzuki, Y. Yamada, J. Polym. Sci. Part B Polym. Phys. 44 (2006) 291–298.
[185] L. Utiu, C. Filipoi, D.E. Demco, X. Zhu, R. Vinokur, O. Conradi, A. Graichen, B. Blümich, M. Möller, Chem. Phys. Lett. 506 (2011) 71–75.
[186] I.L. Moudrakovski, V.V. Terskikh, C.I. Ratcliffe, J.A. Ripmeester, L.-Q. Wang, Y. Shin, G.J. Exarhos, J. Phys. Chem. B 106 (2002) 5938–5946.
[187] S.-J. Huang, S. Huh, P.-S. Lo, S.-H. Liu, V.S.Y. Lin, S.-B. Liu, Phys. Chem. Chem. Phys. 7 (2005) 3080–3087.
[188] S.-J. Huang, C.-H. Huang, W.-H. Chen, X. Sun, X. Zeng, H.-K. Lee, J.A. Ripmeester, C.-Y. Mou, S.-B. Liu, J. Phys. Chem. B 109 (2005) 681–684.
[189] A. Sutrisno, Y. Huang, Solid State Nucl. Magn. Reson. 49–50 (2013) 1–11.
[190] S.B. Choi, H. Furukawa, H.J. Nam, D.-Y. Jung, Y.H. Jhon, A. Walton, D. Book, M. O'Keeffe, O.M. Yaghi, J. Kim, Angew. Chem. Int. Ed. 51 (2012) 8791–8795.
[191] H. Wu, W. Zhou, T. Yildirim, J. Am. Chem. Soc. 131 (2009) 4995–5000.
[192] W. Boehlmann, A. Poeppl, M. Sabo, S. Kaskel, J. Phys. Chem. B 110 (2006) 20177–20181.

[193] T. Ueda, K. Kurokawa, T. Eguchi, C. Kachi-Terajima, S. Takamizawa, J. Phys. Chem. C 111 (2007) 1524–1534.
[194] K. Campbell, K.J. Ooms, R.E. Wasylishen, R.R. Tykwinski, Org. Lett. 7 (2005) 3397–3400.
[195] K.J. Ooms, K. Campbell, R.R. Tykwinski, R.E. Wasylishen, J. Mater. Chem. 15 (2005) 4318–4327.
[196] K. Campbell, K.J. Ooms, M.J. Ferguson, P.J. Stang, R.E. Wasylishen, R.R. Tykwinski, Can. J. Chem. 89 (2011) 1264–1276.
[197] K.J. Ooms, R.E. Wasylishen, Microporous Mesoporous Mater. 103 (2007) 341–351.
[198] S. Pawsey, I. Moudrakovski, J. Ripmeester, L.-Q. Wang, G.J. Exarhos, J.L.C. Rowsell, O.M. Yaghi, J. Phys. Chem. C 111 (2007) 6060–6067.
[199] A. Comotti, S. Bracco, P. Sozzani, S. Horike, R. Matsuda, J. Chen, M. Takata, Y. Kubota, S. Kitagawa, J. Am. Chem. Soc. 130 (2008) 13664–13672.
[200] E. Lima, J. Balmaseda, E. Reguera, Langmuir 23 (2007) 5752–5756.
[201] C. Serre, C. Mellot-Draznieks, S. Surble, N. Audebrand, Y. Filinchuk, G. Ferey, Science 315 (2007) 1828–1831.
[202] G. Ferey, C. Serre, Chem. Soc. Rev. 38 (2009) 1380–1399.
[203] F. Millange, C. Serre, G. Ferey, Chem. Commun. (2002) 822–823.
[204] T. Loiseau, C. Serre, C. Huguenard, G. Fink, F. Taulelle, M. Henry, T. Bataille, G. Férey, Chem. – Eur. J. 10 (2004) 1373–1382.
[205] P.L. Llewellyn, G. Maurin, T. Devic, S. Loera-Serna, N. Rosenbach, C. Serre, S. Bourrelly, P. Horcajada, Y. Filinchuk, G. Férey, J. Am. Chem. Soc. 130 (2008) 12808–12814.
[206] M.-A. Springuel-Huet, A. Nossov, Z. Adem, F. Guenneau, C. Volkringer, T. Loiseau, G. Férey, A. Gédéon, J. Am. Chem. Soc. 132 (2010) 11599–11607.
[207] N. Klein, C. Herzog, M. Sabo, I. Senkovska, J. Getzschmann, S. Paasch, M.R. Lohe, E. Brunner, S. Kaskel, Phys. Chem. Chem. Phys. 12 (2010) 11778–11784.
[208] H.C. Hoffmann, B. Assfour, F. Epperlein, N. Klein, S. Paasch, I. Senkovska, S. Kaskel, G. Seifert, E. Brunner, J. Am. Chem. Soc. 133 (2011) 8681–8690.
[209] N. Klein, H.C. Hoffmann, A. Cadiau, J. Getzschmann, M.R. Lohe, S. Paasch, T. Heydenreich, K. Adil, I. Senkovska, E. Brunner, S. Kaskel, J. Mater. Chem. 22 (2012) 10303–10312.
[210] H. Hoffmann, M. Debowski, P. Müller, S. Paasch, I. Senkovska, S. Kaskel, E. Brunner, Materials 5 (2012) 2537–2572.
[211] F. Hoffmann, M. Fröba, Chem. Soc. Rev. 40 (2011) 608–620.
[212] P.V.D. Voort, D. Esquivel, E.D. Canck, F. Goethals, I.V. Driessche, F.J. Romero-Salguero, Chem. Soc. Rev. 42 (2013) 3913–3955.
[213] A. Comotti, S. Bracco, P. Valsesia, L. Ferretti, P. Sozzani, J. Am. Chem. Soc. 129 (2007) 8566–8576.
[214] A. Silvestre-Albero, S. Rico-Francés, F. Rodríguez-Reinoso, A.M. Kern, M. Klumpp, B.J.M. Etzold, J. Silvestre-Albero, Carbon 59 (2013) 221–228.
[215] C. Galeano, C. Baldizzone, H. Bongard, B. Spliethoff, C. Weidenthaler, J.C. Meier, K.J.J. Mayrhofer, F. Schüth, Adv. Funct. Mater. 24 (2014) 220–232.
[216] F. Rodríguez-reinoso, Carbon 36 (1998) 159–175.
[217] Y. Deng, C. Liu, T. Yu, F. Liu, F. Zhang, Y. Wan, L. Zhang, C. Wang, B. Tu, P.A. Webley, H. Wang, D. Zhao, Chem. Mater. 19 (2007) 3271–3277.
[218] A.-H. Lu, F. Schüth, Adv. Mater. 18 (2006) 1793–1805.

[219] K.V. Romanenko, O.B. Lapina, V.L. Kuznetsov, J. Fraissard, Kinet. Catal. 50 (2009) 26–30.
[220] M. Kruk, M. Jaroniec, T.-W. Kim, R. Ryoo, Chem. Mater. 15 (2003) 2815–2823.
[221] P.A. Simonov, S.V. Filimonova, G.N. Kryukova, E.M. Moroz, V.A. Likholobov, T. Kuretzky, H.P. Boehm, Carbon 37 (1999) 591–600.
[222] K.V. Romanenko, J.-B. d'Espinose de la Caillerie, J. Fraissard, T.V. Reshetenko, O.B. Lapina, Microporous Mesoporous Mater. 81 (2005) 41–48.
[223] C.F.M. Clewett, T. Pietra, J. Phys. Chem. B 109 (2005) 17907–17912.
[224] K.V. Romanenko, A. Fonseca, S. Dumonteil, J.B. Nagy, J.B. d'Espinose de Lacaillerie, O.B. Lapina, J. Fraissard, Solid State Nucl. Magn. Reson. 28 (2005) 135–141.
[225] T. Onfroy, F. Guenneau, M.-A. Springuel-Huet, A. Gédéon, Carbon 47 (2009) 2352–2357.
[226] M. Oschatz, H.C. Hoffmann, J. Pallmann, J. Schaber, L. Borchardt, W. Nickel, I. Senkovska, S. Rico-Francés, J. Silvestre-Albero, S. Kaskel, E. Brunner, Chem. Mater. 26 (2014) 3280–3288.
[227] S.V. Filimonova, H. Knicker, I. Koegel-Knabner, Geoderma 130 (2006) 218–228.
[228] S. Filimonova, A. Nossov, A. Dümig, A. Gédéon, I. Kögel-Knabner, H. Knicker, Geoderma 162 (2011) 96–106.
[229] M. Mauri, R. Simonutti, Materials 5 (2012) 1722–1739.
[230] A. Gedeon, R. Burmeister, R. Grosse, B. Boddenberg, J. Fraissard, Chem. Phys. Lett. 179 (1991) 191–4.
[231] P. Berthault, G. Huber, H. Desvaux, Prog. Nucl. Magn. Reson. Spectrosc. 55 (2009) 35–60.
[232] Q. Wei, G.K. Seward, P.A. Hill, B. Patton, I.E. Dimitrov, N.N. Kuzma, I.J. Dmochowski, J. Am. Chem. Soc. 128 (2006) 13274–13283.
[233] C. Boutin, E. Léonce, T. Brotin, A. Jerschow, P. Berthault, J. Phys. Chem. Lett. 4 (2013) 4172–4176.
[234] M. Zaiss, M. Schnurr, P. Bachert, J. Chem. Phys. 136 (2012) 144106–144106–10.
[235] T.K. Stevens, K.K. Palaniappan, R.M. Ramirez, M.B. Francis, D.E. Wemmer, A. Pines, Magn. Reson. Med. 69 (2013) 1245–1252.
[236] F. Schilling, L. Schröder, K.K. Palaniappan, S. Zapf, D.E. Wemmer, A. Pines, ChemPhysChem 11 (2010) 3529–3533.
[237] P. Berthault, H. Desvaux, T. Wendlinger, M. Gyejacquot, A. Stopin, T. Brotin, J.-P. Dutasta, Y. Boulard, Chem. – Eur. J. 16 (2010) 12941–12946.
[238] J. Roukala, J. Zhu, C. Giri, K. Rissanen, P. Lantto, V.-V. Telkki, J. Am. Chem. Soc. 137 (2015) 2464–2467.

Figure captions

Figure 1 : Historical timeline of ^{129}Xe NMR with important dates and events.

Figure 2. Schematic representation of continuous flow system for production of hyperpolarized ^{129}Xe. From reference [37] with permission.

Figure 3. Schematic representation of polarization transfer from TEMPO radical to Xe nuclei. From reference [76] with permission.

Figure 4. ^{129}Xe NMR spectra of hyperpolarized xenon in calcined aluminophosphate samples after various heating times. The inset in c (after heating for 2 hrs) is an expansion (×10 vertical magnification) of the peak centered at $\delta_{iso} \approx 63$ ppm. From reference [93] with permission.

Figure 5. Left column, ^{129}Xe 2D-EXSY spectra of the sample heated for 24 h at three different mixing times: (a) t_{mix} = 1 ms, (b) t_{mix} = 5 ms, and (c) t_{mix} = 10 ms. The corresponding 1D spectrum collected at the same time as the 2D-EXSY spectra were acquired (32 scans) is shown at the top. Right column, the ^{129}Xe 2D-EXSY spectra of xenon adsorbed in pure AlPO4-18 at two different mixing times: (d) t_{mix} =1 ms and (e) t_{mix} = 5 ms. From reference [93] with permission.

Figure 6. ^{129}Xe NMR spectra of MCM-22 (A) and in ITQ-2 (B) at 293 K for various xenon pressures. From reference [98] with permission.

Figure 7. 2D EXSY MAS NMR spectrum of HP ^{129}Xe adsorbed on ITQ-6 (mixing time 50 ms). Sample was rotated at 3 kHz. $P(Xe) \approx 1.06 \times 10^3$ Pa. Sketch of partially delaminated ITQ-6 particles. From reference [98] with permission.

Figure 8. ^{129}Xe NMR spectra of xenon diffusing in the interpillar structure of TEA-hectorite at variable temperature. From reference [116] with permission.

Figure 9. ^{129}Xe chemical shift as a function of concentration of xenon in samples after acid treatment. (▲) palygorskite, (□) traditional MB and (●) synthetic MB. From reference [120] with permission.

Figure 10. ^{129}Xe CP MAS (upper) and DQ filtered (lower) spectra for Dianin's compound prepared under (a) 1 atm of Xe gas enriched to 99% in ^{129}Xe and (b) 3 atm of Xe gas with natural abundance (26%) ^{129}Xe. The peaks are assigned to xenon atoms located in cavities containing either one or two xenon atoms based on the ^{129}Xe DQ filtered spectra. From reference [122] with permission.

Figure 11. Natural logarithm of the integrated NMR signal intensity ratios, $I_{adsorbed}/I_{gas}$ for materials with Si/Ni = 100 (open symbols) and Si/Ni = 133 (full symbols). Region I, II, III correspond to temperature ranges of 333-235 K, 238-210 K, 212-180 K respectively. Inset: spectra of Ni-133 materials referring to the three regions. From reference [124] with permission.

Figure 12. Schematic representation of three SBA-15s synthesized at (A) 60, (B) 100 and (C) 130 °C, revealing different pore diameters, wall thicknesses, microporosities and interconnections between main channels. From reference [132] with permission.

Figure 13. ^{129}Xe NMR chemical shift versus V/S ratio for aluminas, silica gels and MCM-41. The lines are the nonlinear least-squares fits of the data with equation 2 (section 2.2). From reference [133] with permission.

Figure 14. Schematic representation of the apparent surface (dotted blue line) accessible to Xe atoms diffusing in the mesopores. From reference [133] with permission.

Figure 15. Typical xenon porometry spectra observed for CPG-81, containing Xe and naphthalene, in the different temperature ranges determined by the melting points of the medium. From reference [143] with permission.

Figure 16. Determination of pore size distribution by xenon porometry using a solid medium. The porous material is immersed in a liquid medium, and xenon gas is added to the sample (a). Dissolved xenon atoms (dots) diffuse inside the pores (b). During freezing, empty pockets build up in the pores due to contraction of the medium and xenon squeezes out from the solidifying medium into the pockets (c). The chemical shift of xenon inside the pocket depends on the pore size, and the distribution of the signals observed from the different pores represents the pore size distribution (d). Using the determined correlation (e), the pore size distribution can be obtained by converting the chemical shifts to pore radii (f). From reference [144] with permission.

Figure 17. HP ^{129}Xe NMR spectrum of ZSM-5/Al-SBA-15 composite obtained by partial conversion of the walls of Al-SBA-15 into ZSM-5 zeolite. From reference [145] with permission.

Figure 18. Chemical shift versus Xe pressure of Xe adsorbed in ZSM-5/SBA-15. Adapted from reference [147] with permission.

Figure 19. ^{129}Xe NMR spectra of hierarchical LTA zeolite (NaA-8) and conventional LTA zeolite (NaA-0). Each spectrum was accumulated for 1 d, after xenon contact for 12 h under 1.01×10^5 Pa at 297 K. From reference [150] with permission.

Figure 20. Hyperpolarized ^{129}Xe NMR spectra of Xe adsorbed in MCM-49, in mechanically mixed MCM-49/ZSM-35, in cocrystallized MCM-49/ZSM-35, and ZSM-35 zeolites at 153 and 143 K. From reference [154] with permission.

Figure 21. Continuous-flow hyperpolarized ^{129}Xe NMR spectra of the porous, molecular single-crystal inclined at different orientations θ from 0 to 90° with respect to the magnetic field B_0. From reference [166] with permission.

Figure 22. Top views of polymer columnars (left) and ^{129}Xe NMR spectra (right) of (a) Poly(**Y**), (b) Poly(**R**), and (c) Poly(**B**) at room temperature. From reference [169] with permission.

Figure 23. Comparison between ^{129}Xe NMR data (black solid line, the points show the chemical shifts) and calorimetry data (red dotted line). From reference [172] with permission.

Figure 24. ^{129}Xe NMR chemical shifts of ^{129}Xe in PPO plotted against the Xe pressure at 25 °C. The symbols ◊,●,■ and ▲ are the observed δ, calculated δ and the δ_D (dissolved) and δ_H (adsorbed) components, respectively. From reference [176] with permission.

Figure 25. Xe sorption isotherms of PPO at various temperatures. The solid lines represent the nonlinear least-square curve fit using the dual-mode sorption model. From reference [176] with permission

Figure 26. The framework structures of (A) MOF-123, (B) MIL-246 and (C) MOF-47. From references. [184,185] with permission.

Figure 27. Variable-temperature HP ^{129}Xe NMR spectra for IRMOF-2. Adapted from reference [192] with permission.

Figure 28. ^{129}Xe NMR spectra versus xenon pressure (thermally-polarized ^{129}Xe) recorded at adsorption (A) and desorption (B). From reference [200] with permission.

Figure 29. Chemical shift variations of *lp* (blue) and *np* (red) lines as a function of pressure. Adsorption: full symbols; desorption: empty symbols. Adapted from reference [200] with permission.

Figure 30. ^{129}Xe NMR spectra measured at 237 K and various pressures on DUT-8(Ni) with initially “closed” pore system. The pore system opens at a gate pressure of ca. 12 bar. Adapted from reference [202] with permission.

Figure 31. ^{129}Xe 2D-EXSY map of xenon adsorbed in CMK-3 at 295 K (P_{Xe} = 53 kPa, mixing time = 50 ms). From reference [219] with permission.

Figure 32. ^{129}Xe NMR spectra of the mesoporous sample CMK-3 OM-SiC-CDC-800 before and after loading with n-nonane measured at 237 K at a xenon pressure of 11 bars (p/p0=0.64). From reference [220] with permission.

Figure 33. ^{129}Xe NMR spectra for the barbeque charcoals recorded respectively at P_{Xe}=400 (TP Xe) and 7 mbar (HP Xe). The chemical shift is pressure independent. Adapted from reference [222] with permission.

Highlights

- Introduction to ^{129}Xe NMR of thermally and hyperpolarized xenon
- Comprehensive review of the recent advances in ^{129}Xe NMR
- Reviewing previous work on probing structure interconnectivity of porous materials